Abstract

Neutron reflectometry offers unique benefits for nanolayer research in green chemistry by providing accurate depth profiles of thin films and interfaces with sub-nanometer precision under *in operando* condition of active material in their native environments.   Advantages of this technique include sensitivity to light elements, isotopic contrast control (which enables elemental depth profiles or labelling of specific features or reactants of interest), and the ability to penetrate complex and multimodal sample environments. This chapter focuses on the most stringent example in green chemistry, *in operando* electrochemistry.   Because Neutron Reflectometry is not widely utilized, this chapter provides an introduction, literature review, theoretical basis, practical guides to data collection and analysis, examples, best practices, and future advances, with the goal of making this technique more comprehensible by scientists reviewing or applying Neutron Reflectometry research results and making it more accessible to a wider range of experimenters.

Keywords

Cite as

NANOLAYER ANALYSIS BY NEUTRON REFLECTOMETRY

Joseph A. Dura[1], Eric D. Rus, Paul A. Kienzle, and Brian B. Maranville
NIST Center for Neutron Research Gaithersburg, MD 20899
[1]Corresponding author

צפיפות אורך הפיזור - Ro(n)
מוגדרת על ידי התרכובת, כפונקציה של המרחק מפני השטח

5.1 INTRODUCTION

Neutron reflectometry (NR) measures the nanometer scaled structure of near-surface regions, interfaces, or thin films. Since many green chemistry phenomena involve surface and interface processes, this technique can provide valuable insights into the structures and phenomena that drive or result from these reactions. Specifically, specular neutron reflectometry measures a material property called the scattering length density (SLD) of the neutron or ρ_N, (which is determined from the composition) as a function of depth relative to a surface or interface. Neutrons are particularly sensitive to light elements and can probe interfaces buried in samples, in contact with liquids or deep within complex *in operando* sample environments. Therefore, layered structures often found in green chemistry technologies, such as electrochemical, photo-active, or energy storage devices, can be characterized. This chapter will describe the basis of the technique, concentrating on one of the most stringent, complicated, and comprehensive applications for which NR has been applied to green chemistry: *in operando* electrochemical measurements. Therefore, this chapter will focus on the example of NR as applied to electrochemical systems for green energy storage.

The "contrast" that is observed with NR, *i.e.* the parameter that is described in the structural depth profile, is the scattering length density, $\rho_N(z)$, which is the sum over all the isotopes, *i*, of the

Scattering Length Density = SLD = Ro N ρ_N

bound coherent neutron scattering length, b_c (colloquially, the "neutron scattering power" of the nucleus) times the number density, N, of that isotope:

$$\rho_N(z) = \sum_i b_{c,i}\, N_i(z) \tag{5.1}$$

Here, the depth, z, dependence is specific to specular geometry which (as described in Section 5.2) averages over any variations of ρ_N in the plane parallel to the reflecting interface, but determines variations of ρ_N along the surface normal direction. In the z direction, specular reflectometry is sensitive to layers with thickness ranging from less than 1 nm depending upon the system studied, up to roughly 0.5 µm, depending upon the instrument resolution used. Since the b_c are known for all isotopes, a single measurement can determine composition in systems with two or fewer phases, or in binary alloys if the density vs. composition is known. One of the main advantages of using neutron instead of X-ray or electron probes is that neutrons will scatter from the nucleus, as opposed to scattering from the electrons in a material. First of all, this provides scattering lengths that are alternative and complementary to those probes (which have a low contrast for elements with low atomic number or neighboring elements). Also because neutrons scatter from the nucleus, b_c can vary greatly for different isotopes of the same element, which can be used to determine the depth profile of the number density $N_i(z)$ by comparing the depth profiles determined from samples containing the two different isotopes. Furthermore, by labelling materials of interest with the isotope that has the highest contrast to surrounding materials one can highlight those features. Alternatively, an isotope abundance can be selected to match the contrast of one material to another, (called "isotopic contrast matching") thus eliminating scattering effects from those two materials in order to isolate the scattering from a third material. Finally, isotopic substitution can be used to label one of the reactants to determine the extent to which it contributes to the products that are incorporated into the sample.

Other unique advantages of neutron scattering are derived from the fact that neutrons are weakly interacting particles. Because of this, they are non-destructive, with no ionization or local heating, and can easily penetrate thick solid materials. This promotes both robust *in operando* and multi-modal sample environments since the environment can be tailored to the other technique; for example the neutron can be incident though infrared prisms. Neutrons can also probe the entire sample providing statistical ensemble averages of structures. Scattering from the nucleus eliminates the atomic form factor that must be applied to techniques that probe the electron cloud. With almost zero absorption, the scattering theory is simpler and quantitative, and in fact, the phase problem for diffraction can be solved, allowing inversion of the data if variable reference layers are employed.

Other neutron advantages are less applicable to green chemistry, but are mentioned here for completeness. Because neutrons also have a spin and magnetic moment, they scatter from, and thus are highly sensitive to magnetism in materials. Polarized neutron reflectometry is thus able to determine the depth profile of both the vector magnetization and nuclear ρ_N. In addition, a magnetic layer can serve as the variable reference material required for phase inversion. Finally, because of their large mass, the energy of neutron is similar to that of vibrations, excitations, and diffusion in materials, and the neutron can exchange energy with these modes, in techniques (elastic or quasi-elastic scattering) collectively called neutron vibrational spectroscopy (NVS). NVS is complementary to IR or Raman spectroscopy and is especially sensitive to vibrational modes of H because of its large cross section. Because there are no dipole-selection rules for NVS all vibrational modes are observable. NVS can also obtain the scattering direction in single crystals to obtain phonon dispersion curves, and the length scale of the excitations to help determine the physical mechanism of the vibrations or diffusion.

In specular NR measurements a ribbon shaped beam of neutrons is directed onto the planar sample at a grazing incidence angle, θ, and the reflected intensity is measured as a function of the momentum transfer $\vec{Q}$, which has a magnitude:

$$Q = \frac{4\pi}{\lambda}\sin\theta \qquad (5.2)$$

Diffraction of the neutron from the various interfaces in a material results in variations in the reflected intensity as a function of Q. For a pair of interfaces, i.e. a thin film, this results in an intensity oscillation with a period in Q that is inversely proportional to the thickness of the layer. Multiple layers in the sample produce a beating pattern. Generally, a continuously varying $\rho_N(z)$ can be accurately approximated by a series of thin layers with uniform ρ_N and distinct interfaces, from which the scattering can be determined. Least squares refinement or in some cases direct inversion is used to determine the $\rho_N(z)$ structure of the sample from the reflected intensity, $R(Q)$. Because specular NR requires very flat, smooth samples and averages in the plane, it is not possible to study surfaces, interfaces, or grain boundaries in three dimensional samples, for example between particles in agglomerations. Instead we study planar thin film layers made of the same materials as analogs to those grain boundaries or conformal coatings. These serve as idealized models of the real world interfaces.

The many unique aspects of neutron reflectometry, primarily its proficiency for *in operando* sample environments, sensitivity to light elements, and isotopic control of contrast make it an excellent technique to study electrochemical and other phenomena involving layered structures coatings and ordering at interfaces. Alone or in conjunction with complementary techniques NR will continue to provide useful insights for green chemistry technologies.

5.2 THEORY OF NEUTRON REFLECTOMETRY

5.2.1 Introduction

The wave-like properties of a moving neutron can be used to measure distances, and the nuclear and magnetic interaction potentials to measure materials properties. Combining these properties with the geometry of a thin flat sample, we arrive at the concept of neutron reflectometry. The wavelength of the moving neutron depends on its velocity, through the de Broglie relationship (for non-relativistic particles, wavelength $\lambda = \frac{h}{m_n v}$, where h is the Planck constant, m_n is the neutron mass and v is the velocity). Neutrons with wavelengths close to the inter-atomic spacing are produced at research facilities in order to probe materials at the smallest scales.

There are two types of neutron source for research in common use in the world today: reactor-based and spallation sources. Reactor-based sources are centered around a nuclear fission reactor, in which excess neutrons from the fission process are used, while in spallation sources a high-energy particle beam is focused onto a target, and neutrons are liberated from the nuclei of the target materials through kinetic energy. The particle beam in spallation sources is most often pulsed with time, so that a well-defined burst of neutrons is produced with each pulse, while reactor sources typically operate in a continuous mode where neutrons flow from the source at a nearly constant rate. Spallation sources have the advantage of having a band of wavelengths in each pulse (wavelength within a pulse is determined from the travel time to the detector, inversely proportional to the velocity), thus measuring a range of length scales simultaneously. Because accurate timing and predictable pulses are used, time-resolved probes of materials can be straightforward to set up at a spallation source. Continuous sources provide other optimizations; the time-averaged intensity at particular wavelengths of interest can be much higher than a spallation source, and instrument design can be simplified by not needing time-resolving hardware.

3

No matter which type of source it originated from, the interaction potential for a neutron with matter has two components:

1. The nuclear potential, which depends on the number of protons and neutrons in the nucleus of the atom with which the neutron is interacting. The nuclear potential varies in a non-monotonic way with the atomic number of elements (and isotopes of those elements) in the periodic table.[1] Notably, many lighter elements have strong nuclear potentials (Be, B, C) while heavier elements sometimes are relatively weak scatterers (Co, In, Sm, W) and some are even negative (H, Li, Ti, Mn). A negative scattering length indicates an attractive force between the neutron and nucleus. Compare this to the scattering potential of X-rays with matter, which depends on the electron density of the material, and so X-ray scattering measurements are usually dominated by the heaviest elements present.

2. The magnetic field (B). Scattering only occurs from changes in the vector $\vec{B}$ as a function of z; further, Maxwell's equations applied to thin films dictate that the change in the z-component of B (B_z) along z must be zero, so that B_z is a constant through the film and magnetic NR is only sensitive to changes in the in-plane components B_x, B_y as a function of depth z. Any uniform field (e.g., the applied external magnetic field, for example) does not contribute to the scattering, which arises only from the magnetic potentials due to the material itself, such as in ferromagnets or ferrimagnets, or in superconducting thin films which create magnetic discontinuities through the Meissner effect.

5.2.2 Specular Theory

The theory of specular scattering can only be completely solved for films that are uniform in-plane. In reality, the theory works quite well for samples that have relatively small contrast variations in-plane, or samples where this contrast has a much smaller length scale than the coherent extent of the neutron wavefunction during the interaction with the sample (e.g. interatomic variations in SLD in-plane, nanoscale porosity or domains etc.) For most samples that can be described as layered thin films it works quite well; on the other hand, very strong in-plane contrast such as from a ruled grating on a surface [2] makes this analysis moot and computationally-intense approximations are required.

If we go back to the de Broglie relationship mentioned earlier, we can write down a wavefunction for the neutron: $\psi(z) = ce^{ikz} + de^{-ikz}$, where k is the wavevector along z, related to the momentum as $\hbar k = p_z = m_n v_z$ for non-relativistic velocities v. The change in the momentum of the neutron due to the scattering is $\vec{Q} = \vec{k}_{out} - \vec{k}_{in}$, and Q is often used as the independent variable that is changed in a reflectometry experiment. On the actual instrument, Q is controlled through a combination of sample angle and incident wavelength, since $Q = \frac{4\pi}{\lambda} \sin\theta$ where λ is the wavelength and θ is the angle of incidence of the neutron on the sample. At a reactor source, the angle is typically varied for a fixed wavelength, while at a spallation source a spectrum of wavelengths is typically incident at just a few fixed angles.

The form above of the wavefunction ψ has the correct wavelength as specified by de Broglie. The coefficients c and d correspond to the amplitudes of the forward- and backward-traveling waves. If we apply conservation of momentum, conservation of energy, and conservation of particle number at each of the boundaries between layers of the sample, we can write down a series of equations for the amplitude of the neutron wavefunction in each layer.

In the incident medium (the material through which the neutron travels to reach the first interface of the sample) we know that $c_0 = 1$ and $d_0 = r$, because the wave traveling toward the sample c is our incident flux which we normalize to 1, while the backward-traveling wave there is the reflection that we measure, r. In every subsequent layer l there is a value of $\{c, d\}_l$ which can be determined by enforcing conservation of particle number across the boundary $\psi_l(Z_l) = \psi_{l+1}(Z_l)$ where Z_l is the interface

4

between layers $l, l+1$, and also by enforcing conservation of momentum with the simultaneous equation $\frac{d}{dz}\psi_l(Z_l) = \frac{d}{dz}\psi_{l+1}(Z_l)$. Using conservation of energy, we can get an equation for k_l, the wavevector in the next layer, by keeping the sum of kinetic and potential energy the same:

$$E_0 = K.E. + P.E. = \frac{1}{2}m_n v_l^2 + \frac{\hbar^2}{2m_n}4\pi\rho_{n,l} = \frac{\hbar^2}{2m_n}\left(k_l^2 + 4\pi\rho_{n,l}\right) \tag{5.3}$$

where $\rho_n = \rho_N + \rho_M$ is the scattering length density for neutrons (the sum of nuclear and magnetic components).

So if we know the scattering length density of a layer, $\rho_{n,l}$ then

$$k_l = \sqrt{\left\{\frac{2m_N}{\hbar^2}\right\}E_0 - 4\pi\rho_{n,l}} \tag{5.4}$$

Note that this gives an imaginary value for k_l when the scattering potential in the material exceeds the incident energy $E_0 = \frac{\hbar^2}{2m_n}k_0^2 = \frac{\hbar^2}{2m_n}\frac{Q^2}{4}$. Then the wavefunction inside the layer is a decaying exponential rather than a plane wave, though the transmitted amplitude through the layer can still be large if the layer is thin compared to the decay length (quantum tunneling of the particle wavefunction!) If the layer with imaginary k is thick enough, (such as the substrate) the transmission goes to zero and there is total external reflection. In this case the measured reflectivity R is 1: Every neutron that hits the sample is reflected. This happens for Q below the point we call the critical edge $Q_c^2 = 16\pi\rho_n$, which is where k_l in the high-SLD layer goes through zero (and then is imaginary).

    The two boundary-value equations for ψ give two equations for the two unknowns c and d in the next layer, allowing us to calculate c_{l+1}, d_{l+1} based on the values c_l and d_l in the previous layer. Arranging these equations as a 2x2 matrix we get:

$$\binom{c}{d}_{l+1} = \frac{1}{2k_{l+1}}\begin{pmatrix} (k_{l+1}+k_l)e^{-i(k_{l+1}-k_l)Z_l} & (k_{l+1}-k_l)e^{-i(k_{l+1}+k_l)Z_l} \\ (k_{l+1}-k_l)e^{+i(k_{l+1}+k_l)Z_l} & (k_{l+1}+k_l)e^{+i(k_{l+1}-k_l)Z_l} \end{pmatrix}\binom{c}{d}_l \tag{5.5}$$

The off-diagonal matrix elements that connect the forward-traveling wave amplitudes c to the backward (reflected) wave amplitudes d are proportional to the difference in k between one layer and the next, which in turn depends on the difference in SLD at that interface. For large values of E_0 (high angle in a reflectometer) the difference in k at an interface becomes roughly linearly proportional to the difference in SLD, so that the amplitude of the high-angle reflectivity is a measure of the SLD contrast that caused it, while oscillations in the reflectivity are caused by interference between the reflected waves from interfaces at different depths. For a single layer, the reflections from the top and bottom of the layer will interfere destructively whenever $k_l\times(\Delta z)_l = \left(n+\frac{1}{2}\right)\pi$, so that the period of the oscillations (particularly at high Q) is roughly equal to $\Delta Q \approx \frac{2\pi}{\Delta z}$.

If we call the matrix above A_l (including the prefactor $1/2k_{l+1}$), we can write an equation that traverses all the layers as a product of the A_l, getting c_l and d_l in terms of the incident intensity 1 and reflected amplitude r (still unknown):

$$\binom{c}{d}_L = \left[\prod_{l=L}^{0}(A_l)\right]\binom{c}{d}_0 \tag{5.6}$$

5

Note that the product moves in reverse order through the indices l of the layers.

    In the final layer (usually the sample substrate, if there is one, or the same material as the incident medium for a free-standing film) there is one more boundary condition: We can identify the forward traveling wave amplitude c_L as the transmission amplitude often called t, which is a measurable quantity like r, but also we know that for the experimental setup there is no backward-traveling wave (other neutron source) coming from that side, so that $d_L = 0$, where L is the total number of layers (including the incident and transmission media). Then we have two equations and we can solve for the two unknowns, t and r (where $[M = \prod_{l=L}^{0} A_l]$ from above)

$$\begin{pmatrix} t \\ 0 \end{pmatrix} = M \begin{pmatrix} 1 \\ r \end{pmatrix} \tag{5.7}$$

So

$$t = M_{11} + M_{12}r \tag{5.8}$$
$$0 = M_{21} + M_{22}r$$

Solving gives

$$r = -\frac{M_{21}}{M_{22}} \tag{5.9}$$

$$t = M_{11} - 1\frac{M_{12}M_{21}}{M_{22}}$$

One can immediately see that for a single interface, this reduces to the familiar Fresnel reflectivity $r = (k_0 - k_1)/(k_0 + k_1)$.

    Note that while the theory is derived for a series of slabs of constant ρ_n, any smooth depth profile for the SLD can be accurately approximated as a series of thin slabs. The thickness of the slabs can be made arbitrarily small without affecting the validity of the theory, although below a certain threshold (roughly calculated from the measured Q-range as $\frac{2\pi}{Q_{max}}$) no accuracy in the model is gained by further reducing the thickness.

    The amplitudes t and r above are complex numbers containing phase information. The measured quantities (reflectivity R and transmission T) are the square of the amplitudes $|r|^2$ and $|t|^2$, and all phase information is lost in the measurement.

5.2.3 Phase recovery

    For any scattering experiment such as reflectometry, the measured quantity (in this case, R) is a real number with no phase information, so the matrix equations described above cannot be directly inverted to get a unique solution to the layer-by-layer scattering length density. There are some experimental tricks we can employ to recover that information, though. If we have perfect knowledge of the scattering length density of the media surrounding the sample of interest, and we can vary that SLD, the mathematical constraints from this knowledge can be used to construct a series of equations where the phase is recovered. This technique is described in the literature.[3]

    The most commonly used methods of altering the media in a known way is to substitute pure D_2O for H_2O in a liquid reservoir that abuts the sample, or flipping the magnetization of a magnetic underlayer which changes the SLD by a known amount for a polarized neutron (polarized neutron techniques described elsewhere).[4] The technique only works when there is no appreciable absorption in the sample, which makes it a more useful tool in neutron scattering than in X-ray scattering, where the absorption is much larger.

5.2.4 Isotope substitution

Another useful strategy for extracting unambiguous real-space information from the scattering data is isotope substitution. One can achieve a targeted measurement of the density profile of a particular element by exchanging a particular atomic component of a material for a different isotope of the same element, in an otherwise identical structure. Then the difference in SLD (see Eq. (5.1)) as a function of depth, divided by the difference in $b_{c,i}$, is a direct measure of the distribution of that element. Because the exact location of this contrast in the SLD profile is unknown ahead of time, the data cannot be directly inverted with this strategy alone, but the two techniques (isotopic substitution and surround variation to achieve direct inversion) can be combined, of course.

5.2.5 Near-specular techniques

While the specular technique is an elegant solution for measuring uniform, flat samples, sometimes the sample of interest has some kind of in-plane structure, while still resembling mostly a thin-film structure. In this case, one must consider the scattering in more than just one dimension; unfortunately, there is no closed-form solution to the more general 3D scattering problem as there was for the 1D case above. Two near-surface scattering techniques in common use include:

1. GISANS, which is essentially SANS (small-angle neutron scattering) where the incident beam is at or below the critical angle of total external reflection, θ_c, for the sample. By small variation in the incident angle then, the user can tune the penetration depth of the evanescent probe wave that tunnels into the sample; through a series of measurements a depth-dependent, in-plane scattering picture can be built up. GISANS covers a Q-range in-plane that is similar to the out-of-plane direction.

2. Off-specular scattering, in which the instrument geometry is largely unchanged from the specular case, but the sample is tilted so that the momentum-transfer vector Q has a small in-plane component. Because of the very small angles of incidence involved, the range of Q_x (in-plane) that is covered is small but very good precision is achievable, and long-range-ordered structures with repeat distances of hundreds of microns can be resolved.[2] While it is possible to measure with extremely high Q-resolution, the max Q_x that is attainable with reasonable scattering intensity is much smaller than specular Q_z-range.

5.3 PRACTICAL ASPECTS

Neutron reflectometry can provide precise and accurate structural information for features as small as sub-nanometer thickness under ideal conditions. However, in order to accurately achieve this level of precision, numerous practical aspects must be carefully attended to. These issues are addressed in this section, and range from sample preparation, sample environment (including electrochemical cell) construction, instrument use and data collection and reduction, to (not least importantly) selection and validation of models and data fitting. Best practices, and the reasons behind them are presented to provide the reader the basis to obtain useful NR results or when evaluating research to distinguish the accuracy of measurements.

5.3.1 Neutron reflectometers

A basic understanding of a neutron reflectometer is necessary to both correctly and optimally collect data and to understand sample and cell design requirements. The specific design of neutron reflectometers differs slightly based on the type of instrument, for example time of flight reflectometers at pulsed beam[5] or continuous beam spallation sources,[6] monochromatic[7] or proposed polychromatic reflectometers (similar to polychromatic diffractometers[8]) at continuous beam, reactor-based sources. However, there are numerous similarities, and where differences exist there are typically analogues in the other techniques. Therefore, in the interest of brevity, to convey the concepts of how a reflectometer

7

works, the simplest form, a monochromatic reflectometer, will be described herein, with some of the more important differences with the other types pointed out.
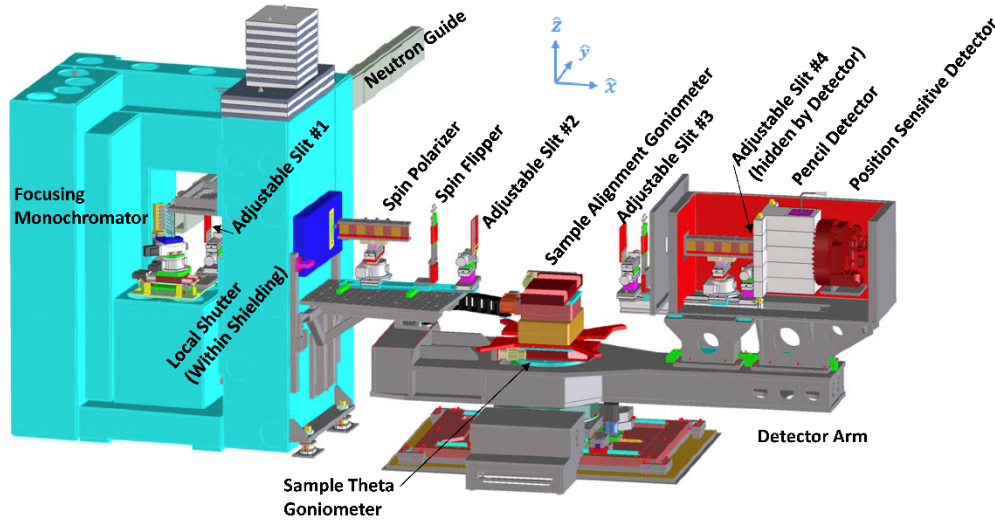

Fig. 5.1: Neutron reflectometer at a continuous source with major components labelled. Axes are shown for ease of discussion.

Fig. 5.1 shows a typical monochromatic reflectometer with a horizontal scattering plane and thus a vertical sample surface, often called a vertical sample reflectometer (further details can be found in the literature[7]). For ease of discussion, the coordinate system is as shown with "z" in the vertical direction and "y", which rotates with the sample, along the bisector of the incident and reflected beams. A focusing monochromator is placed in a gap in the neutron guide to diffract a nearly monochromatic beam ($\Delta\lambda/\lambda = 0.015$) at a right angle from the guide for neutrons with a wavelength $\lambda = 0.4743$ nm; however, other angles and wavelengths can be used. A cryogenically cooled Be filter in the incident path removes neutrons with a wavelength under ~0.39 nm, particularly the λ/n higher orders that would otherwise also be diffracted by the monochromator into the beam direction. A vertical slit near the monochromator and another near the sample define a beam that is narrow and has small angular divergence in the horizontal plane (which is needed to provide high resolution for the incident angle, θ, and to control the area of the sample that is illuminated. The monochromator is curved to provide vertical focusing to allow a greater flux on the sample. An adjustable aperture is placed near the sample to better define the vertical extent of the beam. While the vertical focusing increases the beam divergence in this direction (relative to having a flat monochromator), this is orthogonal to theta, and therefore minimally increases the resolution along the specular direction. The only issue with a large vertical divergence is that it can integrate off specular scattering, if present, into the specular signal. Because the incident beam is fixed in space, the incident angle θ is set by rotating the sample on a goniometer, and similarly the reflected angle, D, is set by rotating the detector. For specular scattering $D = 2\theta$, both the θ and D axis must be concentric and vertical, and intercept the beam to an accuracy of a few 10's of micrometers for typical reflectometers. A pair of slits, one just after the sample and the other just before the detector along the line between sample and detector, define the reflected beam and limit the acceptance to a region near the sample, to reduce the background signal. Each slit is composed of two blades of a neutron-absorbing material with an adjustable gap between them (called the slit width), but with a center point that is fixed to provide a stationary beam path and a fixed wavelength. Typically, a beam monitor is placed intercepting a portion of the incident beam at some point along its path and is used to normalize the incident intensity against variations in source flux over time. A

8

cylindrical ^{3}He type detector is typically used. This must be tall enough to intercept the diverging beam from the focusing monochromator. Alternatively, the detector slits can be removed and a position sensitive detector can be installed to allow efficient measurements of off-specular scattering.

As a final note on neutron reflectometers, because acceptable neutron fluxes can only be achieved at specialized facilities (reactor or spallation sources) rather than lab based neutrons sources, NR experiments require travel to user facilities, of which there are currently 23 major ones throughout the world.[9] This in itself imposes additional constraints on experiment design. There is usually a significant lead time for proposals to be written, reviewed, and for beam time to be awarded and scheduled. There are limited opportunities for follow-on experiments or corrections. Therefore it is often helpful to precharacterize the samples to ensure that the structures are as desired and of sufficient quality, then to model the expected data to investigate the sensitivity of the measurements to the phenomena of interest. Most user facilities have instrument scientists to provide varying degrees of support from simply providing access through collaboration, which is a great advantage since it allows new users to learn a new technique while ensuring valid measurements.

5.3.2 Data Collection

The objective of an NR measurement is to accurately and precisely quantify the reflectivity, which is the specularly reflected intensity divided by the incident intensity as a function of incidence angle, which is often expressed as Q. To accurately determine the angle, sample alignment is crucial. The sample must be aligned to the common rotation axes of the sample and detector goniometers (to which the beam is already aligned) with precision to several micrometers. These axes must lie on and bisect the surface of the sample that is to be measured. The sample surface normal must also be aligned along the momentum transfer vector, $\vec{Q}$. Alignment begins with the detector placed in the incident, direct beam, and the sample is translated along y until the surface intersects the beam as indicated by a dip in intensity due to a reflection. Then θ is scanned and set to the value for the maximum transmitted beam. Finer alignment is achieved by setting the detector angle just below the critical edge of the sample to obtain total reflection, and adjusting θ, y and χ (the rotation about the horizontal axis in the plane of the sample surface) to maximize the intensity of the reflected beam. This defines θ as half of the value of D that was used.

Data is typically collected with step scans where the sample angle, detector angle, and slit openings are driven to the desired values and the reflected intensity is counted on the detector and monitor for a specified amount of time (or counts on the monitor or detector), then repeated for a range of theta values. Typically, the incident slits are increased linearly with θ to keep the beam footprint on the sample constant, to provide a constant $\Delta Q/Q$, and a flux that increases as Q^2, to partially offset the Q^{-4} dependence of R for reflectivity from a plane. The amount of time per point is also increased with Q to provide adequate counting statistics for the reduced reflectivity with increasing Q. However, at low angles where slit motor precision becomes a significant fraction of the slit opening and at higher angles where the slit opening approaches the detector width, a fixed slit opening can be used. The specular condition is maintained by setting the detector angle to twice the sample angle, and although this includes both specularly reflected neutrons and isotropically scattered neutrons as well as other sources of background, it is called the specular scan. For convenience, the Q-range of interest can be divided into a series of separate specular scans. In situations where the sample structure might change during the course of an experiment, this possibility should be checked by taking several series of specular data (over either the full or limited Q-range), retaining only those scans for which the sample does not change. Measuring a sample that is changing over time could result in misinterpretation of the structure because the time average reflectivity curve does not correspond to the scattering from the time average structure. If the data were taken by scanning Q with time, the oscillations and Bragg peaks would shift with time, and each Q would correspond to a different structure, fitting the whole NR pattern would not

9

correspond to any particular sample structure. For example, shifts in oscillation maxima due to a changing sample thickness could appear as a beating pattern in the oscillations which in turn would be interpreted as a thin layer that does not exist in the sample. Even if all Q were measured simultaneously (as with time of flight reflectometers) changes in sample thickness would shift the phase of intensity oscillations, and time averaging, especially at higher Q would broaden the oscillations, making the interfaces appear more diffuse than otherwise.

Since non-specular scattering also occurs at the specular conditions this and other sources of background must be accurately subtracted from the total intensity that was measured in the scan of the specular condition. This is achieved by offsetting either the sample or detector angle until the specular beam no longer enters the detector. Typically, this is done symmetrically on both sides of the specular condition (to account for possible gradients in the background intensity) and the average is used.

Finally, the incident intensity as a function of slit settings (and wavelength in polychromatic instruments) must be determined. This is typically done by taking a "slit scan" through the sample environments and incident media, but with the sample surface displaced from the beam, in which the detector is placed in the direct beam and the intensity is measured for the full range of slit settings used in the specular reflectivity measurement.

To determine R vs. Q, the background is subtracted from the specular data, which is divided by the slit scan. The counting statistics of these individual measurements are propagated through the reduction to provide uncertainty estimates for each data point. If fixed slits are maintained at low Q, the beam may be wider than the projection of the sample surface onto the plane perpendicular to the beam (YZ). This gives rise to a $\sin \theta$ (roughly linear) increase in intensity for the reflected intensity (proportional to the fraction of the beam intercepted by the sample, called the footprint) up until the point where either the sample fully intercepts the beam or where slits are opened in proportion to θ. A "footprint" correction can be applied if necessary. The sample is often not perfectly planar at the level of beam divergence which can be on the order of 0.01 degree, either due to polishing errors, or warping due to film deposition, other processing, stresses applied by the sample holder or cell. Therefore, the reflected beam can be broadened by the sample. This will affect both the downstream slits openings needed to accept the full specular beam, and will round off the footprint profile, which can affect the choice of slit settings below the critical edge.

5.3.3 Data Fitting

Like diffraction, it is the intensity not amplitude that is measured in reflectivity, so the phase of the probe wave function is lost and the data cannot be analytically inverted to determine the SLD profile that gives rise to the pattern in the reflected intensity. Instead, the SLD profile is usually determined by defining a model of the expected structure (typically a series of layers described by the complex SLD, the thickness, and amount of intermixing and profile shape at each interface), and adjusting the model parameters until the predicted reflectivity matches the data. Since most thin film samples consist entirely of intentionally placed layers, this approach is simple and direct, typically the parameters vary a limited amount from the expected values. However, in electrochemical systems layers may be generated without *a-priori* knowledge of their composition and structure, or in some cases without knowledge of even the number of distinct layer units. Therefore, in many of the systems of interest to this chapter, one does not even know what model will best describe the sample and considerable effort must be employed to determine the appropriate model while at the same time determining the best fit parameters. In general, the model definition (in terms of fitting) includes not only to the number of layers, but also the values of fixed parameters and the fitting ranges. Model selection in cases with an unknown structure is complicated by the fact that it is mathematically possible that two symmetry related SLD profiles can result in exactly the same NR curve.[10]

10

Several approaches can be applied to reduce the number of unknowns, both to provide accurate determination of the remaining parameters, and to also help determine the best model to describe the data. External probes can provide a great deal of complementary information. These can characterize the actual sample investigated with NR before and / or after the NR experiment to further define the initial and final states. Alternatively, samples can be prepared in the same manner and studied at each of the conditions also examined by NR, thus determining the model and restricting the parameter ranges to reflect sample to sample deviations. The most useful probes to help in model selection are those that also provide a depth profile, even if they lack the sensitivity or resolution of NR, for example XRR, RBS, cross sectional electron microscopy, or sputter depth profiling coupled with compositional probes such as XPS, SIMS or SNMS.

There are several NR methods that can be applied to assist in model selection and fitting. If the initial sample consists of multiple layers, one can measure NR or XRR, x-ray reflectometry, at various stages of sample layer deposition to determine the layer parameters in simpler systems as the layers are added (though be aware that the underlayers can change over time depending on the deposition method). The inversion methods specific to neutron reflectometry (see Section 5.2.3) use information from a set of measurements with a reference layer set to different SLD values to directly invert the data. Reference layers can be a fluid reservoir, where fluid exchange controls the contrast, or a magnetic layer, where polarized neutron reflectometry provides different total SLD for the different polarizations. Simultaneously fitting the same pair of data sets will also resolve the symmetry issues, while allowing prior information from complementary measurements to constrain them.[11] Two samples that are prepared identically but with different isotopes for one component (isotopic substitution) can be used to determine the number density depth profile of that element, and to help verify that a correct model has been employed. Finally, if these methods are unavailable there are approaches that can be taken during fitting to determine the best model. For example, a series of models with different number of layers can be used to fit the data and the Bayesian Information Criteria, BIC, can be applied to determine the best fit among varying models.[12] Models can be underdetermined, characterized by a relatively poor fit and high χ^2, or overdetermined indicated by a low χ^2 and possibly strong correlations between parameters, but ultimately by a higher BIC than models with fewer parameters and similar SLD profiles.[13] Free-form modelling where the depth profile is described by a set of orthogonal basis functions has also been demonstrated.[14] Combined models, with structured layers for the well-defined parts of the structure and free-form sections where model composition is not well controlled, provide additional flexibility.

There are certain limitations on what can be determined from neutron reflectometry. Since the period of oscillation in Q space is inversely proportional to the thickness of a layer, a feature may be too thin to produce an observable oscillation in the data. Therefore, in general, a lower limit for observable feature size is $2\pi/Q_{max}$, where Q_{max} is the largest Q for which the data has reasonably small error bars. In some cases, smaller features can be inferred from the data, for example if a certain contrast at an interface (which does not exist for the layers that are observable, being thicker than $2\pi/Q_{max}$) is required to fit an oscillation amplitude, but cannot be achieved by the SLD of the other adjacent layers due to known materials properties or the fitting. However, in these cases, extreme care must be used to demonstrate that such a contrast is actually required. Similarly, an upper limit on the thickness of a layer is set by the resolution of the instrument, $2\pi/Q_{min}$, where Q_{min} is the smallest oscillation period that is not obscured by instrumental broadening. Models must be evaluated for realism; the SLD values determined by the fits must correspond to what is possible given the materials in the system. SLD values lower than what is expected for bulk materials can be explained by lower density or porosity. Interdiffusion from adjacent layers can explain SLD values either lower or greater than bulk, within reasonable limits dictated by mass balance.

When fitting, one must be diligent in evaluating whether the returned best fit is actually the global minimum in χ^2 or is merely a local minimum. Gradient decent approaches can easily get stuck in

11

the nearest local minimum, but restarting the fit from numerous different initial conditions can increase the chances of finding the global minimum. The more robust but slower Monte Carlo approaches can ideally find the global minimum, and can also be used to determine a likelihood band for the model parameters, but even they have difficulty in distinguishing between different local minima with similar χ^2. See [Section 5.4](#) for more details.

5.3.4 Sample Requirements

Both X-ray reflectometry, and neutron reflectometry have similar sample requirements. First, samples must be very flat. Deviations from planarity, generically referred to as "warp" regardless of the cause, broaden the effective instrumental resolution by increasing the range of incident angles upon the sample. Warp also increases the divergence of the reflected beam, requiring increased downstream slit width and thus decreasing signal to noise ratio. It also distorts the profile of the reflected intensity vs θ in the region before the sample intercepts the entire beam, making footprint corrections more difficult to apply, or alternatively decreasing the maximum initial beam width required to avoid these corrections.

Samples must also have smooth surfaces and interfaces (approximately less than 2 nm RMS or more depending on the system), since roughness increases the overall rate of decline in R vs. Q, faster than the typical $R \sim Q^{-4}$ for smooth planer surfaces, thus decreasing signal to noise faster than otherwise. Interfacial roughness also decreases oscillation amplitude (by increasing amounts at higher Q), decreasing sensitivity to layers (or equivalently, in real space, distributing thinner layers over a larger depth range, thus averaging their distinct composition over larger regions and decreasing the ability to distinguish thin layers.)

Because of the relatively low fluxes of neutron sources, sample area should be maximized (up to the limits of the beam size) to maximize the signal and minimize the time required for adequate counting statistics. However, film thickness must also be uniform across the film (typically < 2% variation) since separate regions of the sample with various thickness each would produce different oscillation periods. These are measured simultaneously and incoherently averaged over, effectively broadening the oscillation and decreasing its amplitude increasingly with higher Q in a manner similar to the effects of interface roughness, for which it can be mistaken in the fits. On a smaller scale, in-plane inhomogeneities smaller than the projection of the neutron coherence length[2] onto the sample surface, ~1μm/sin θ, are averaged over. For larger inhomogeneities the measured intensity is an incoherent combination of the reflectivity from each component of the inhomogeneity. If the number of different lateral components are known the data can still be analyzed, though with greater uncertainty. This requires a set of models of the depth profile for each lateral component of the inhomogeneity and a weighting parameter proportional to the relative area of that component. Except in the simplest and most well defined cases this becomes unsolvable due to the large number of fitting parameters and the decrease in information content of the R vs. Q due to averaging over multiple different NR curves.

Cells that contain a liquid reservoir typically require the neutrons to be incident through the substrate. At some angle the neutron beam will transition from being incident though a substrate edge to being incident through the back of the substrate. This should be avoided by using thick enough substrates (on the order of several mm) to avoid unnecessary scattering from the substrate edge and a change in incident angle due to a change in refraction of the beam. Electrochemical processing can induce stress in layers and materials, including adhesion layers, and processes must be chosen to avoid delamination. Surface oxides, even on the nanometer scale, that can develop upon exposure of the prepared thin film to the atmosphere can drastically effect both the electrochemistry and the scattering, and must be taken into account. Relatively smooth films can be produced by sputtering, however in some cases the ion energy can lead to interdiffusion, or penetration of the sputtered material through existing layers, such as the native oxide on Si.[15]

12

While avoiding these pitfalls, the intentionally deposited thin films can be customized to provide advantages. The thickness of all layers and composition of the adjacent layers should be chosen to differ from the values of the layer expected from the electrochemical effect being tested, to avoid ambiguous interpretation of features in the NR data and to provide adequate contrast. In some cases, the underlying structures can be designed to actually enhance the sensitivity to those layers. Modeling the NR data produced by the potential underlying structures can be used to optimize the sensitivity to the phenomenon to be measured, and to demonstrate this sensitivity in proposals for beam time at neutron facilities.

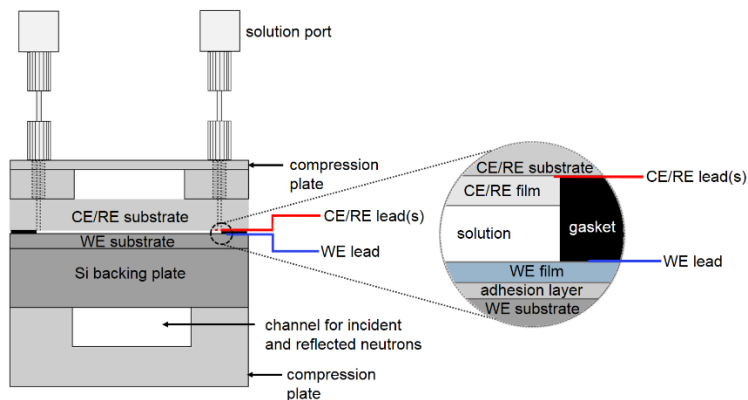### 5.3.5 In operando NR / Electrochemical Cell Design Considerations

Fig. 5.2 Schematic cut away view of an in situ NR electrochemical cell (not to scale), with magnified view to show greater detail.

In operando/in situ NR compatible electrochemical cells for battery materials have been described previously[13,16,17,18,19,20,21], and in other articles by the same groups. Since neutrons are weakly interacting due to their charge neutrality, they can readily penetrate single crystals, but are highly attenuated in amorphous materials and liquids (due to scattering from the liquid structure) and in particular from materials containing H (due to incoherent scattering). Therefore, all NR electrochemical cells operate in a back-reflection configuration, using a single crystal substrate (commonly silicon, quartz, or sapphire), which supports the working electrode (WE), as the incident medium. Refractive effects are avoided by directing the beam through the side of the substrate which is perpendicular to the sample surface. Thus the substrate itself must be sufficiently thick to accommodate the range of incident angles. This thickness is also useful in minimizing warp due to the stresses induced by sealing the cell. Additional thickness can be added by stacking another substrate of the same material behind the WE substrate. However, the WE substrate should be thick enough that any reflection from its back surface occurs at adequately high angles that the reflectivity of the substrate is very weak. This reflection can be minimized by using unpolished surfaces and ensuring that there is no contamination, such as electrolyte, between the WE substrate and the additional backing plate. At the NCNR, 5 mm thick, 76.2 mm diameter silicon substrates are typically used. With a 2.6 mm maximum beam width, this condition begins at $\theta = 5.55°$ or $Q = 2.5$ nm^{-1}, and no anomalies are observed there in either the specular or background scans.

The electrolyte reservoir can be sealed with a thin gasket or O-ring. In one commonly used cell type, referred to herein as "thin cells," the counter electrode (CE) is a film deposited onto a substrate similar to that used for the WE, and placed directly against the other side of the gasket[13,17,18,19,20,21,22] (see Fig. 5.2). The thickness and inner dimensions of the gasket thus define the electrolyte reservoir volume. Minimizing the volume is important for several reasons. First, large volumes increase the absolute amount of contaminants (such as water) even for small concentrations. For a cell containing 1

13

mL of solution, one monolayer of contamination would correspond to a solution contaminant concentration on the order of 1×10^{-8} mol/L. Also, deuterated solvents (which are very useful for controlling scattering length density contrast by mixing with natural isotopic abundance solvents, for measuring porosity, and for tagging reactants of interest) can be expensive, so minimizing both the reservoir volume and the volume required to fully exchange the fluid can be economically essential. The latter benefits from a uniform, non-turbulent, flow front in addition to the small reservoir volumes. Care must be taken, however, that the counter electrode does not contribute to the reflected signal, for example, by having a solution volume sufficiently thick to absorb or scatter the beam transmitted through the working electrode. Furthermore, the reservoir thickness should be greater than the projection of the longitudinal coherence length[2] of the neutron in that direction (~100 μm) so that any scattering that does occur is incoherent with the scattering from the working electrode. This must be balanced however with the desire to minimize the background scattering, which is achieved by both minimizing the thickness of the reservoir and by using deuterated solvents. Fortuitously, in the case of lithium ion measurements, a sufficiently thick lithium foil counter electrode will absorb most of the neutrons in the beam (though care must be taken in the disposal of the lithium, since ^{6}Li is converted to tritium by neutron absorption). In liquid cells without a lithium counter electrode, an unpolished side of a wafer is typically faced towards the reservoir, decreasing its reflectivity.

Thin cells have been made either with or without fluid inlets. In the latter case, the gasket is placed on top of one electrode, and solution added to the reservoir, then second wafer is lowered onto this, taking care not to trap any bubbles. Alternatively, inlets can be provided via holes drilled through the counter electrode substrate. Tubing can then be sealed to the back side of the counter electrode substrate with O-rings, gaskets, or tube fittings such as those used for HPLC.

In another cell type, the reservoir is defined by a cavity within a structure that seals against the WE with the gasket or O-ring. Such "cavity cells" have been constructed from glass,[17] PTFE,[16,23] and polyethylene.[24] The primary advantage of a larger cavity is that it allows a conventional reference electrode to be located within the reservoir between the WE and CE. It also facilitates incorporation of fluid inlets. The counter electrode can be a macroscopic sheet, wire, or gauze. Yonemura *et al.* employed a hybrid approach in which the cavity in an aluminum body was only 0.5 mm thick except for two ~5 mm diameter inlet holes machined perpendicular to the WE surface, one that also housed a combination CE/RE.[21]

The CE should have the same area as the WE to ensure uniform potential distribution, since non-uniform effects on the sample structure across its surface would incoherently contribute different reflectivity vs Q to the measured reflected intensity and prevent accurate modelling of the sample structure. Care must be taken that the CE reactions do not produce significant volumes of gas, as bubbles could become trapped in the gap. Not only would this lead to inhomogeneity in the electrochemical reactions at the working electrode, but the SLD of gas bubbles will most probably differ from the SLD of the solution, leading to lateral inhomogeneities of the sample. Furthermore, small bubbles would produce small angle scattering, leading to increased background. Also, given the long duration of NR measurements, species produced at the counter electrode have ample time to diffuse across the gap and could potentially react at the working electrode. While a separator could slow this crossover, it would undesirably contribute to scattering at the working electrode/solution interface.

Platinum is commonly used as a counter electrode in aqueous media, and compensates charge passed at the working electrode either by oxidizing or reducing water. While platinum is quite stable, some soluble platinum species can form with the passage of current, and particularly under conditions where an oxide layer is repetitively formed and reduced.[25] For lithium ion measurements, lithium foil is most commonly used as the counter electrode. Lithium metal adheres fairly readily to glass and quartz, and to ground surfaces in particular, and counter electrodes can be prepared by pressing foil against the substrate with a roller.

14

A reference electrode (RE) can be incorporated in several ways. A conventional RE can be installed in the thick reservoir of a cavity cell. Alternatively, it can be installed in a "T" in one of the fluid inlets or can be placed in a dedicated cavity in the counter electrode substrate for a shorter path to the reservoir. A thin wire quasi/pseudoreference electrode can also be inserted directly into the reservoir, but these are potentially less accurate/reproducible than a conventional RE and more susceptible to drift since potential is not poised by a well-defined redox couple.

The type of reference should be chosen on a case by case basis, depending upon compatibility with the system under consideration. The Ag/AgCl electrode is a convenient reference to use in aqueous media, but either the system must be tolerant of chloride contamination, or measures (*e.g.* use of a cation selective membrane) must be taken to prevent chloride from reaching the working electrode. Given the long time scales of NR measurements, there would be time for significant amounts of chloride to diffuse out of the reference. Chloride specifically adsorbs on metal electrodes, meaning it can adsorb in preference to other less strongly adsorbing species, even when present at far lower concentration. The reactivity of an electrode surface with adsorbed chloride may differ significantly from that of an electrode surface free from specifically adsorbing anions. There are other aqueous references, such as the saturated calomel electrode (SCE), Hg/Hg_2SO_4, Hg/HgO, and hydrogen electrodes (RHE, DHE, SHE/NHE), which are described in detail elsewhere.[26]

One possible reference for non-aqueous measurements is the Ag/Ag^+ electrode.[26] For non-aqueous lithium ion electrolytes, a piece of metallic lithium can typically be used as a reference electrode. Very commonly, measurements in lithium ion electrolytes are carried out in a two electrode configuration, with a single sheet of lithium serving as both the reference and counter electrode. Such two electrode measurements are valid only so long as the polarization of the combined reference/counter electrode is minimal. While its placement is not ideal,[27] one possible method of incorporating a lithium reference electrode is to adhere an additional piece of lithium to the counter electrode substrate in a location separate from the counter electrode (assuming the counter electrode substrate is an insulator).

The structure holding these components together should be electrically isolated from the working and counter electrodes and must be designed such that no additional material is placed in the direct and reflected beam paths in order to avoid background scattering and signal attenuation, respectively. An additional useful feature is to have a transparent component, either the counter electrode and its substrate (*e.g.* using a quartz substrate) in thin cells or a window in the cavity cells, to allow observation of the working electrode in case of bubble formation or delamination. It is important to confirm that all materials in contact with the electrolyte are chemically compatible. This includes the lining of inlet holes drilled in the CE substrate, all sealing materials, tubing for solution ports, and even adhesion layers under the working and counter electrodes, since those electrodes can become porous during an experiment. The material used to make electrical contact to the CE must either be stable within the potential range over which the CE polarizes, or must not come into contact with solution. Particular care must be taken that the current collector/lead used to make electrical contact to the WE is not in contact with the solution, otherwise the lead will contribute to the observed electrochemical behavior, producing ambiguous results. Due to the long times required for NR measurements, the cell should be tested before the experiment for similar amounts of time to determine if the structures are stable. Also the WE should be checked after this test for delamination or in plane non-uniformity.

In the case of cells containing lithium or other sensitive materials, assembly should be carried out in a glove box or dry room to protect the reactive components from atmospheric gases. Lithium will react with oxygen, nitrogen and carbon dioxide. Additional protection can be added during the NR measurements by placing the cell in an enclosure with flowing inert gas. The material used for the neutron windows on this enclosure should be selected to minimize neutron absorption and scattering. Thin aluminum sheet functions adequately in this role.

15

5.4 MODERN DATA ANALYSIS

As mentioned previously, it is typically not possible to invert reflectometry data, so we must fit the data to determine the SLD profile. Since we can exactly calculate the reflectivity from a given SLD profile as described in Section 5.2, we can adjust the parameters for the profile until we have the best fit to the data. We approach this from the Bayesian perspective, wherein we calculate the likelihood of seeing the measured data for a given set of parameters, and adjust the parameters to maximize this likelihood. This approach allows us to incorporate prior information into the fitting process and to understand the uncertainty in the resulting fit parameters. In Section 5.4.1 we show that this approach is equivalent to traditional least squares and describe some practical algorithms for finding the maximum likelihood. In Section 5.4.2 we show how we can compute uncertainty on the fitted parameter values.

5.4.1 Maximum Likelihood Analysis

Consider what it means to perform a measurement. Given some control stimulus x, a system f characterized by parameters $\boldsymbol{b}$ produces response D. The purpose of the measurement is to infer the properties $\boldsymbol{b}$ from the response, *i.e.*, given $D = f(x, \boldsymbol{b})$, determine $\boldsymbol{b}$. The measurement process is not perfect, with the measured response D only being known with some uncertainty which can best be represented as probability distributions $P(D)$. There will be some information about the system from previous measurements, so $\boldsymbol{b}$ will have a prior probability $P(\boldsymbol{b})$. This is refined by the measurement to produce the posterior probability $P(\boldsymbol{b}|D)$, which is the probability of $\boldsymbol{b}$ updated by the information from the measurement D. (The control stimulus x also has uncertainty, but this is usually very small and can be ignored or incorporated into the model f.) Using the joint probability of two events A and B both occurring, $P(A, B) = P(A|B)P(B) = P(B|A)P(A)$, we can derive Bayes' Rule for probabilistic inference. Applying this to the measurement question $P(D, \boldsymbol{b})$, we get

$$P(\boldsymbol{b}|D) = \frac{P(D|\boldsymbol{b})P(\boldsymbol{b})}{P(D)} \tag{5.10}$$

That is, if we can compute the probability of observing measured value D for system parameters $\boldsymbol{b}$ then we can combine that with prior information about $\boldsymbol{b}$ to refine our estimate of the probability of $\boldsymbol{b}$. The $P(D)$ term is a constant independent of $\boldsymbol{b}$, so we can form the maximum likelihood estimate using $\hat{\boldsymbol{b}} = \max_{\boldsymbol{b}} P(\boldsymbol{b}|D) = \max_{\boldsymbol{b}} P(D|\boldsymbol{b})P(\boldsymbol{b})$. Assuming normally distributed measurement uncertainty, $P(D|\boldsymbol{b}) \propto e^{-\chi^2/2}$ where $\chi^2 = \sum_i r_i^2(\boldsymbol{b})$ for weighted residual $r_i(\boldsymbol{b}) = (f(x_i, \boldsymbol{b}) - D_i)/\Delta D_i$, and no prior information so $P(\boldsymbol{b})$ is constant, then $-\ln P(\boldsymbol{b}|D) = \chi^2/2 + C$ and traditional least squares optimization $\hat{\boldsymbol{b}} = \min_{\boldsymbol{b}} \chi^2$ determines the Bayesian maximum likelihood estimate.

The Levenberg-Marquardt (LM) algorithm[28] is a very efficient method for minimizing χ^2 in a non-linear system. Using the $n{\times}m$ Jacobian matrix $\boldsymbol{J}$ with $J_{ij} = \frac{\partial r_i}{\partial b_j}$ for data point i and fitting parameter b_j, the LM algorithm updates an initial estimate $\boldsymbol{b}_0$ using

$$\boldsymbol{b}' = \boldsymbol{b} + (\boldsymbol{J}^T\boldsymbol{J} + \lambda \operatorname{diag}(\boldsymbol{J}^T\boldsymbol{J}))^{-1}\boldsymbol{J}^T\boldsymbol{r}(\boldsymbol{b}) \tag{5.11}$$

The parameter λ controls the type of update step, ranging from the first order gradient descent method for large λ to the second order Gauss-Newton method for small λ. If the proposed step $\boldsymbol{b}'$ is an improvement with $\chi^{2\prime} < \chi^2$ then we are approaching the minimum, so favor the second order method by decreasing λ, setting $\lambda \leftarrow \lambda/10$ for the next iteration; keep the improved point by setting $\boldsymbol{b} \leftarrow \boldsymbol{b}'$. If the step is worse, then reject it, leaving $\boldsymbol{b}$ unchanged and bias the next iteration toward the more robust first order method by setting $\lambda \leftarrow 10\lambda$.

Because the LM algorithm only uses the gradient and curvature at the current point to determine the next point, it is a purely local optimizer and can fail on complex fit spaces. As layer thicknesses in

16

reflectivity models change, the peaks and valleys of the reflectivity signal go in and out of phase with the data, leading to many widely separated local minima in χ^2, so LM is unlikely to find the global minimum from an arbitrary starting point. Since we cannot even be sure that we have the correct model to describe the system, we need robust optimizers, only using LM to perform quick fits at the beginning of the analysis and "finishing" fits at the end.

The LM algorithm, which requires that f be a sum of squares, is only useful for χ^2 minimization, and not for full Bayesian analysis with arbitrary prior information about the fitting parameters. Even simple bounds on a fit parameter, which corresponds to a uniform prior probability $P(b_k)$ for the parameter b_k within a range, is not supported by LM. More general Gauss-Newton and gradient descent optimizers such as BFGS can operate directly on the negative log likelihood function $-\ln P(\boldsymbol{b}|D)$ using numerical derivatives, but these are still local optimizers that suffer from the robustness issues of the LM algorithm. Also, care is needed when handling parameter bounds, since the derivative is not defined at the boundary. The Nelder-Mead simplex algorithm,[29] while still a local optimizer, does not directly use the gradient and so is less drawn toward the nearest minimum and can handle more complex constraints but has slower convergence. Differential evolution (DE) is still more robust, using population-based search to traverse the parameter space $\boldsymbol{b}$.[30] DE selects a pair of points $\boldsymbol{b}_i$ and $\boldsymbol{b}_j$ from the population, defines the difference vector $\delta\boldsymbol{b} = \boldsymbol{b}_i - \boldsymbol{b}_j$, projects this onto a random subspace by setting components to zero with probability CR (or "crossover ratio"), scales by a factor F near 1 and applies the resulting vector to a third point $\boldsymbol{b}_k$ producing

$$\boldsymbol{b}'_k = \boldsymbol{b}_k + F\delta\boldsymbol{b}_{CR} \tag{3.12}$$

If the step is an improvement, so that $P(D|\boldsymbol{b}'_k)P(\boldsymbol{b}'_k) > P(D|\boldsymbol{b}_k)P(\boldsymbol{b}_k)$, then point k is updated using $\boldsymbol{b}_k \leftarrow \boldsymbol{b}'_k$. While still a "descent" algorithm in that it only accepts parameter sets that improve the likelihood, the population $\{\boldsymbol{b}_i | i = 1, \dots, n\}$ tunes itself to the space $\boldsymbol{b}$, collecting in the minima. This works well for reflectivity problems, allowing DE to jump between the quasi-regular minima in the probability density.

The most robust algorithms are not strictly descent algorithms, but are instead able to take steps to lower probability points in the parameter space. With many iterations they can take enough "bad" steps to climb out of a local minimum and drop into another one. Simulated annealing[31] uses the notion of temperature T, with the probability of taking the step from $\boldsymbol{b}_i$ to $\boldsymbol{b}_j$ as

$$\alpha_{ij} = \begin{cases} e^{-\Delta E}/T, & \Delta E > 0 \\ 1, & \Delta E \leq 0 \end{cases} \tag{5.13}$$

The ΔE term is the log probability ratio

$$\Delta E = \ln \frac{P(D|\boldsymbol{b}_j)P(\boldsymbol{b}_j)/P(D)}{P(D|\boldsymbol{b}_i)P(\boldsymbol{b}_i)/P(D)} = \ln \frac{P(D|\boldsymbol{b}_j)P(\boldsymbol{b}_j)}{P(D|\boldsymbol{b}_i)P(\boldsymbol{b}_i)} \tag{5.14}$$

The selection of the test point $\boldsymbol{b}_j$ given the current point $\boldsymbol{b}_i$ must be random, selected from some "proposal distribution" q with $q_{ij} = P(\boldsymbol{b}_j|\boldsymbol{b}_i)$ giving the probability of selecting $\boldsymbol{b}_j$. This could be as simple as picking a random direction in the n-dimensional parameter space and stepping a random distance, $\boldsymbol{b}_j = \boldsymbol{b}_i + F\boldsymbol{b}/|\boldsymbol{b}|$ for random F and $\boldsymbol{b}$, or it could use an adaptive step such as the $F\delta\boldsymbol{b}_{CR}$ update from DE. Simulated annealing also needs an "annealing schedule", which starts at high temperature allowing easy movement between minima, and then lowers with each iteration until the algorithm is strictly descending and converges to the local minimum. The annealing schedule may include temperature increases, allowing the algorithm to cycle between searching for the nearest minima and then allowing it to escape to nearby minima.

17

5.4.2 Uncertainty Analysis

Parameter uncertainty can be characterized by integrating over the posterior distribution $P(\boldsymbol{b}|D)$ using Markov chain Monte Carlo analysis (MCMC). Consider the sequence of points at each iteration of simulated annealing, including duplicates if the proposed point is rejected. When run at a constant temperature $T = 1$ with steps chosen from proposal distribution q which preserves the "detailed balance" condition $q_{ij}\alpha_{ij}\pi_i = q_{ji}\alpha_{ji}\pi_j$,[32] the sequence forms a Markov chain with the remarkable property that it will eventually reach a steady state wherein the elements $\boldsymbol{b}_i$ of the chain appear with probability π_i. That is, using $\pi_i = P(D|\boldsymbol{b}_i)P(\boldsymbol{b}_i)/P(D)$ the sequence $\boldsymbol{b}_1, \boldsymbol{b}_2, \ldots$ will be a "random draw" from the posterior distribution $P(\boldsymbol{b}|D)$. (Since $P(D)$ is constant it cancels when computing ΔE, so we only need $\pi_i \propto P(D|\boldsymbol{b}_i)P(\boldsymbol{b}_i)$.) With randomized DE as the proposal distribution, the resulting DREAM algorithm[33] provides the framework for robust optimization with uncertainty analysis. Unlike many other MCMC algorithms, the DE proposal distribution is self-adaptive so the DREAM algorithm can be applied to many different problems with very little parameter tuning.

Given the sequence of points generated by MCMC, we can use Monte Carlo integration with importance sampling to estimate a number of statistical properties of the fitted parameters. Importance sampling allows us to compute the integral $\int f(\boldsymbol{b})\pi(\boldsymbol{b})d\boldsymbol{b}$ by selecting points $\boldsymbol{b}_i$ from $\pi(\boldsymbol{b})$ and summing $f(\boldsymbol{b}_i)$ over all points. Since points from high probability regions are more likely to appear in the sequence those regions will contribute more to the sum, implicitly weighting $f(\boldsymbol{b})$ by $\pi(\boldsymbol{b})$. More formally, given a random draw S from $x \in \mathbb{R}^n$ with probability $\pi(x)$,

$$S = \{x_i | i = 1 \ldots N\} \text{ with } P(x_i \in S) = \pi(x_i) \tag{5.15}$$

then

$$\hat{I} = \int_{\mathbb{R}^n} f(x)\pi(x)\, \mathrm{d}x \approx \frac{1}{N}\sum_i f(x_i) \tag{5.16}$$

with variance

$$\mathrm{Var}(\hat{I}) \propto \frac{1}{N} \tag{5.17}$$

So if we have enough samples S from $P(\boldsymbol{b}|D)$ we can estimate the following to arbitrary precision:
- the expected value, or mean of parameter b_k as

$$\langle b_k \rangle = \int_{\mathbb{R}} b_k P(b_k|D)\, \mathrm{d}b_k = \int_{\mathbb{R}^n} b_k P(\boldsymbol{b}|D)\, \mathrm{d}\boldsymbol{b} \approx \frac{1}{N}\sum_i b_k[i] \tag{5.18}$$

  Here, $b_k[i]$ is the value of parameter k from point i in the set S. The resulting average is "marginalized" across the entire joint distribution $P(\boldsymbol{b}|D)$, including any correlations between the parameters that might favor some values of b_k over others.
- the variance of parameter b_k as

$$\sigma^2 = \int_{\mathbb{R}} b_k^2 P(b_k|D)\, \mathrm{d}b \quad b_k^2 P(b_k|D)db_k - \mu^2 \approx \frac{1}{N}\sum_i b_k[i]^2 - \mu^2 \tag{5.19}$$

  Using estimated mean $\hat{\mu} = \langle b_k \rangle$ instead of the true mean μ, the usual correction of $N/(N-1)$ is required to remove the bias in sample variance.
- the probability density histogram as a set of integrals plotted as a bar chart, with width 2Δ and probability $p(x)$ as

18

$$p(x) = \int_{x-\Delta}^{x+\Delta} P(b_k|D) \, db_k \approx \frac{1}{N} \sum_{x-\Delta < b_k \leq x+\Delta} 1 \tag{5.20}$$

The 2-D correlation histogram is similar, but using pixels rather than bars.

- the $1 - \alpha$ credible interval as (x_l, x_r) where

$$\int_{-\infty}^{x_l} P(b_k|D) \, db_k = \int_{x_r}^{\infty} P(b_k|D) \, db_k = \frac{\alpha}{2} \tag{5.21}$$

which can be estimated by $\left(b_k \left[\frac{N\alpha}{2} \right], b_k \left[N - \frac{N\alpha}{2} \right] \right)$ for sorted b_k. This extends to all quantiles q including the median $q = 0.5$, which can be approximated using $b_k[Nq]$.

- the $1 - \alpha$ shortest credible interval as (x_l, x_r) from

$$\min_{x_l < x_r} x_r - x_l \text{ such that } \int_{x_l}^{x_r} P(b_k|D) \, db_k = 1 - \alpha \tag{5.22}$$

which can be estimated as $x_r - x_l = \min_i (b_k[N(1 - \alpha) + i] - b_k[N\alpha + i])$ for sorted b_k. This estimate will be biased low and should only be used for large sample sizes.

- the maximum likelihood value $\widehat{\boldsymbol{b}}$ as the value with the highest probability; the value $\min_i - \ln P(b_i|D)$ should be close to the maximum likelihood value, and is an excellent starting point for the Gauss-Newton algorithm to find the best fit. Note that the best fit is an accident of the measurement. If you were to repeat the experiment with an identical sample in the identical environment, you would measure slightly different $R(Q)$ and find a different maximum likelihood value, but the credible intervals should remain mostly unchanged.

- a random sample as a subset of S. Random samples can be useful for example to generate a set of typical scattering length density profiles from the fit and compute a 68% confidence band. The subset should be selected at random to avoid short distance correlations between points in the Markov chain.

The quality of the estimated values depends not only on length of the Markov chain, but also upon its quality. If the DREAM algorithm is stopped too soon, then the Markov chain may not have converged, and sample set will be skewed toward the initial guess. This will be visible as a gradual reduction in the average $P(\boldsymbol{b}|D)$ value with each generation. The points from this "burn-in" period cannot be used for subsequent analysis, and are thrown away. For particularly difficult problems, the DREAM algorithm may become stuck and show poor "mixing", so instead of well-behaved chains which quickly traverse the high density regions of the posterior probability $P(\boldsymbol{b}|D)$, many consecutive samples on each chain will remain at the same value. Sometimes "thinning" the chain by only keeping 1 in 10 samples will help in this situation, but usually it requires constraints on the search space, such as limiting the fit range or reducing the number of fitted parameters.

The correlation histograms are particularly useful for understanding uncertainty in the model parameters. The ideal situation would show circular patterns for every pair of parameters, indicating that every parameter is independent of every other parameter. A correlation between parameters will appear as a diagonal on the parameter-parameter plot. With the reflectivity interference pattern highly dependent on the overall thickness, these can appear as a trade-off between the thickness of one layer with another. If there are many correlations, this can be a sign of an overly complex model, with the extra degrees of freedom trading amongst each other, and so the number of layers should be reduced.

19

More complex correlations can appear, especial with constraints between the parameters. Although rare in reflectivity modeling, multiple solutions will appear as disconnected blobs in the correlation plots. For example, in small angle scattering models with ρ_f and ρ_s as the SLD for the particle and the solvent respectively, the intensity $I(Q) = \Delta^2 V^2 F^2(Q)$ is proportional to the square of the contrast $\Delta = \rho_{N,f} - \rho_{N,s}$ so identical scattering will appear for $\rho_{N,f} = \rho_{N,s} + \Delta$ and $\rho_{N,f} = \rho_{N,s} - \Delta$. When fitting $\rho_{N,f}$ using DREAM with no prior probability restricting $\rho_f > \rho_s$, the returned fit will show equal probability for each solution. Similarly, when applied to a crystallography problem in which symmetries were not removed, DREAM was able to return the four equally probable solutions within the fit range.[34] The demonstrated ability of DREAM to return multiple widely separated minima in a multi-dimensional search space provides confidence that it is able to find the global minimum.

The Refl1D[35] software package from the NCNR includes support for the various optimization methods found in this section, including LM, BFGS, Nelder-Mead simplex, DE and DREAM. MotoFit[36] from ANSTO provides LM and DE.

5.5 CURRENT EXAMPLES

Neutron reflectometry has been applied to electrochemical systems for green energy including batteries, supercapacitors, and fuel cells. These energy conversion and storage technologies most often rely upon light nuclei, *i.e.* hydrogen and lithium, to which neutrons are particularly sensitive relative to photon and electron based techniques. In studying these interfaces, NR has been used to detect the formation/presence of surface layers, to measure layer porosities, thickness changes, water (or solvent) uptake, and diffusion rates through layers. After an overall review of these applications, three specific examples will be presented to highlight in greater detail some of the techniques that make NR of particular value to studies of electrochemical energy storage and conversion.

5.5.1 General Review of many types of Green energy applications
5.5.1.1 Li-ion Batteries

Amongst the presently available battery chemistries, Li-ion batteries offer the highest energy density. This makes them particularly attractive for consumer electronics and automotive applications. Their high energy density is achieved by the use of anodes poised at extremely reducing potentials and cathodes poised at highly oxidizing potentials. The anode and sometimes the cathode potentials are poised outside the thermodynamic window of stability of the solvent and electrolyte.[37,38] Without the formation of a passivating layer, referred to as the solid electrolyte interface (or interphase) (SEI),[39] at the solid-liquid interface, continuous breakdown of the solution would occur, and the battery would rapidly fail. Major aims of battery research are to improve the energy density, safety, and cycle life of Li-ion batteries, and the nature of the SEI plays an important role in all of these aspects.

The importance of understanding the SEI is evident in the gamut of techniques that have been used in characterizing it.[38,40] Characterization of the SEI is challenging as it is highly sensitive to the ambient atmosphere, and removing an SEI-coated electrode from a cell for *ex situ* measurements could alter it, as even trace levels of oxygen can oxidize these nanometer-scale films. Even if the electrode is kept in an inert atmosphere between being removed from the cell and being characterized, washing procedures could also alter the SEI, *e.g.* by removal of material or collapse of porosity.[41] Thus, *in situ* measurements are of great value. Techniques including FTIR spectroscopy, electrochemical quartz crystal microbalance, cantilever surface stress measurement, x-reflectometry,[42,43] ellipsometry,[44,45] scanned-probe techniques, and others have been used for *in situ* characterization. The SEI consists mostly of light element-containing compounds, to which neutrons show greater sensitivity/specificity than other probes. Neutron reflectometry is also sensitive to the nanometer-scale thickness of the SEI.

Several groups have recently used NR to characterize SEI formation on electrodes including titanium dioxide,[46] copper[20], carbon[47], and silicon[24,48,49,50,51,52] as model anodes, and on lithium iron

20

phosphate,[23,53] lithium manganese nickel oxide,[22] lithium manganese nickel oxide,[22] and lithium cobalt oxide[54] cathodes.

5.5.1.1.1 Li-ion Battery Anodes

Anatase In the study of lithium intercalation in an anatase TiO_2 thin film, the nature of the phase boundary between lithium titanate and lithium anatase phases was investigated.[46] The phase front was found to be parallel with the surface throughout reduction and oxidation, with a model showing the titanium oxide layer splitting into two layers of differing SLD during reduction. This model was taken to support lithium ion diffusion across the anatase/lithium titanate phase boundary as the rate limiting step. Another possible mechanism considered was for the phase transformation to proceed heterogeneously (*e.g.* propagating fastest along grain boundaries and then spreading out laterally from these boundaries). The layer model proposed for this mechanism showed the SLD of the titanium oxide layer changing homogeneously (since reflected neutrons would average out lateral inhomogeneity). This model was found to be a worse fit than that in which the oxide layer bifurcated, so the latter was preferred. Additionally, it was noted that there was an additional surface layer, interpreted to be an SEI, on an electrode that had been reduced and oxidized once. The oxidation and reduction of anatase proceed at about +1.8 V *vs* Li/Li^+. This material could be considered a high-potential (safer) anode, or possibly as a low-potential cathode.

Copper Owejan *et al.* were the first to apply NR to systematically characterize the evolution of the SEI layer as a function of potential and number of cycles in an experiment specifically designed to emphasize the SEI.[20] Cu was chosen as a working electrode since it alloys essentially no Li and thus all the changes to the NR could be associated with the evolving SEI layer and all the accumulated charge could be associated with the electrolyte breakdown. A 4 nm SEI was found to form after 10 potential cycles, and evolve in thickness, composition, and uniformity with depth as a function of the cell potential. This study will be described more fully as one of the three detailed examples to follow.

Carbon Carbon (graphite) is the anode used commercial Li-ion cells at present. Preparation of model carbon electrodes presents a challenge because deposition of thin graphite films typically results in the graphitic planes parallel to the surface, rather than the more technologically interesting plane edges through which the Li intercalates. While other types of carbon can have significant capacity,[55] SEI growth on these may differ from that on graphite. Kawaura *et al.* prepared amorphous carbon thin films on a titanium adhesion layer by magnetron sputtering.[47] Fitting of *in operando* NR data indicated a 21% expansion of the carbon layer and a decrease in its SLD when sweeping the electrode potential from open circuit potential to 0 V *vs* Li/Li^+, which was attributed to lithiation of the carbon. The model also included an interfacial layer, interpreted to be the SEI, which approximately doubled in thickness during the negative-going potential sweep. Inclusion of an interfacial layer in the model was needed even for fitting the data at open circuit. Based upon the decrease in the SLD of the carbon layer, it was determined that about 25% of the total reduction charged passed went into SEI formation, though this calculation did not take into account the possibility of co-intercalation of ^1H-containing species (solvent molecules) along with lithium ions, as graphite may do.[56,57]

Silicon Silicon is presently of interest as a high capacity anode material, (3580 mAh/g on a pre-lithiated basis for a $Li_{3.75}Si_1$ stoichiometry) and has been the focus of several NR studies.[24,48,49,50,51,52] Silicon undergoes a volume expansion of up to 300% upon lithiation,[58] which is particularly demanding on the SEI, which must expand with the electrode or be broken to allow expansion of the electrode. The latter may allow for further SEI formation (and irreversible lithium sequestration) with the electrode surface re-exposed to solution.

21

In an initial study, Jerliu *et al.* measured NR of an amorphous silicon thin film electrode at open circuit, and after each of three periods of galvanostatic reduction (lithiation) and two periods of oxidation (delithiation).[24] No SEI/reaction layer formation was noted at open circuit. With reduction, the silicon layer thickness increased and its SLD decreased, as would be expected. During oxidation, the layer contracted, returning to the initial thickness to within error, and its SLD increased. The silicon film SLD did not return to a value as high as the original value, indicating some lithium remained in the layer. Interestingly, while an SEI was not detected after reduction, it was present after oxidation.

In a subsequent study, Jerliu *et al.* used NR to measure changes in this thickness of an amorphous silicon thin film at several points during electrochemical lithiation.[48] A more limited range of Q_z was used to shorten the data acquisition time to enable to collection of more data sets. Fitting of the data showed the thickness did not change in the initial stages of lithiation, though no explanation was offered for this. At higher degrees of lithiation, a linear relation of thickness with degree of lithiation was shown, with a slope of about 0.8 (V/V_0)/stoichiometric equivalent of Li. This value was found to be consistent between 40 nm and 140 nm silicon films, and also between the first and second cycles. After the 40 nm electrode was reduced, it was re-oxidized galvanostatically. Its thickness after oxidation was 60 nm, indicating the reduction process was chemically irreversible, and that some lithium remained in the film. The limited Q_z range made it impossible to discern whether any gradients in lithium concentration existed within the film, or whether an SEI was present.

An initial study by Veith *et al.* investigated the non-electrochemical reaction of an amorphous Si surface with an electrolyte consisting of a $LiPF_6$ solution in a mixed dimethyl carbonate/ethylene carbonate.[49] Measurements of the as deposited sample in air indicated a 2.3 nm thick surface layer attributed to a sub-oxide or contamination. The sample was then soaked in the electrolyte, washed in dimethyl carbonate, and finally assembled into a liquid cell in contact with deuterated cyclohexane. In this state the surface layer of 3.5 nm thickness appeared, consuming both the former 2.3 nm layer and 1.8 nm of the Si layer (which decreased from 76.5 nm to 74.7 nm in thickness) Also, fitting of NR data from the bare electrode showed a lower than theoretical SLD of the silicon film, suggested that the film contained 5% void space, which was further substantiated by another measurement in which the film was immersed in deuterated cyclohexane.

In subsequent work Veith *et al.* measured NR of an amorphous silicon film electrode.[51] A 4.5±0.5 nm SEI/reaction layer with a $(2.4\pm0.5)\times10^{-4}$ nm^{-2} SLD formed at open circuit, accompanied by consumption of some of the silicon layer as this became thinner when placed in contact with the electrolyte (decreasing from 66.3±0.1 nm in air to 59.3±3 nm in solution at open circuit).[59] The reaction layer was taken to be formed from the $LiPF_6$ rather than the solvents as its SLD was significantly lower than that of the deuterated solution (4.6×10^{-4} nm^{-2}). An initial process observed during galvanostatic reduction was assigned to the reduction of an impurity, possibly HF, and resulted in an increase of the surface layer thickness to 17.5±3.5 nm, with a SLD of $(4.7\pm0.3)\times10^{-4}$ nm^{-2} which is similar to that of the solvent. With further cycling, the SEI thickness was found to decrease with reduction and increase with oxidation, although both changes were within one standard error. Based on the fitted SEI SLD, it was concluded that the SEI had higher LiF content at low potentials and higher Li-C-O-F content at higher potentials.

Most recently the same group studied the behavior of a silicon thin film electrode in a solution consisting of a novel dimethyl perfluoroglutarate solvent and a bis(trifluoromethanesulfonyl)imide electrolyte.[41] While this solution has significantly lower conductivity than typical Li-ion electrolytes, it could be prepared with higher purity than commercially available deuterated solvents, it has a relatively high scattering length density and low incoherent scattering. Also, it may be stable to higher potentials than conventional carbonate solvent-based solutions, have lower flammability, and good SEI characteristics. No SEI/reaction layer was detected at open circuit, but a 14.4±3.2 nm SEI with a SLD of $(4.5\pm0.1)\times10^{-4}$ nm^{-2} (slightly below that of the electrolyte SLD of 4.78×10^{-4} nm^{-2}) formed upon

22

reduction to +0.7 V *vs* Li/Li$^+$. The SEI thickened to 26.6±2.1 nm with a SLD of $(4.7\pm0.1)\times10^{-4}$ nm^{-2} after reduction to +0.4 V. Further cycling of the electrode showed the SEI to contract during reduction and swell during oxidation. *Ex situ* XPS measurements on another electrode indicated the opposite: contraction of the SEI during oxidation and swelling during reduction. The discrepancy was attributed to loss of weakly bound species from the SEI upon removal from the cell and washing, highlighting the value of performing measurements *in situ*.

DeCaluwe *et al.*[50] used NR to study a thin film amorphous silicon electrode covered with an aluminum oxide protective layer. The protective layer acts as an artificial SEI providing ionic conductivity while being electronically insulating, thus preventing direct contact of the solution with the electrode and preventing SEI formation. This simplifies the system under study since the changes should then only be due to bulk transformation of the silicon layer and not changes to its surface. It was found that in the initial stages of lithiation, the silicon layer thickness did not increase significantly, though it did in later stages of lithiation (as seen in the earlier studies). The pore collapse and regrowth, PCRG, mechanism was proposed wherein expansion of the silicon layer first proceeded by isotropic expansion of the silicon to fill void space initially present in the layer. Once the void space was filled, the layer expanded anisotropically along the surface normal. When the electrode was re-oxidized, the silicon layer first receded along the surface normal anisotropically, and then the void space regrew. Addition of an SEI layer to the model used to fit the data did not improve the quality of the fit, indicating the AlO$_x$ layer was effective at preventing SEI formation.

A different approach taken recently by Seidlhofer, *et al.* was to use a bulk sample consisting of a conductive (0.005 Ω cm) phosphorous-doped single crystal silicon <100> wafer as the electrode, rather than an amorphous thin film over a Li-blocking substrate.[52] At open circuit, a 2 nm thick reaction layer with a SLD of 1.87×10^{-4} nm^{-2} was present on the surface over the native SiO$_2$. The wafer was subjected two cycles of galvanostatic reduction and oxidation, while NR was measured between 0.07 nm^{-1} and 0.63 nm^{-1} at 5 minutes/pattern. Upon galvanostatically reducing the electrode, a layer of SLD lower than that of the solution, presumably due to enrichment of Li in the phase, formed over the native silicon oxide. With continued reduction, the Li-enriched layer and the native oxide were removed, and a decrease in the silicon SLD penetrating about 50 nm into the bulk was then noted. This lithiated layer consisted of a 20 nm-thick skin region of higher lithium content (with a calculated Li$_{2.5}$Si stoichiometry), and a second region of lower lithium concentration (Li$_{0.1}$Si) extending beyond this into the bulk. The limited depth to which the lithium penetrated into the bulk may be attributed to the build-up of stress limiting further lithiation. Some lithium remained in the bulk upon reoxidation of the electrode as was indicated by the presence of a 3 nm thick layer with a 0.56×10^{-4} nm^{-2} SLD, corresponding to about Li$_{1.1}$Si. Additionally, a 3.6 nm thick surface layer with a 1.99×10^{-4} nm^{-2} SLD, taken to be the SEI, formed during oxidation. The changes in the NR during the second cycle of galvanostatic reduction and oxidation were similar to those in the first cycle, again showing the formation of a more heavily lithiated skin layer and a more dilute lithiation region extending further into the bulk. The SEI that had formed during the first oxidation step was removed during the second reduction, though it formed again during the second oxidation.

The larger number of studies of the Si surface allows some trends to be observed. A surface layer/solid electrolyte interface was noted in some of these studies.[24,41, 49, 51,52] In one of the cases in which it was not observed, it could have been present but not detectable due to the limited range of Q_z measured,[48] and in another case the presence of a protective layer over the silicon prevented SEI formation.[50] In the cases in which an SEI was detected, one group observed it to form during oxidation following an initial reduction,[24, 52] while another group observed it to form during the initial reduction.[41,51] It was suggested that the difference was possibly due to differing experimental conditions, *e.g.*: rate at which the electrochemical reaction was driven or the supporting electrolyte used. The formation of a reaction layer at open circuit was noted in some cases,[49,52] which may be produced

23

by a reaction between the solution and a preexisting oxide or contamination layer present on the as-prepared film. There is a general consensus that no expansion occurs for low Li concentration in amorphous Si, which, in the absence of contamination, can be explained by the PCRG mechanism.[50]

In addition to these *in situ* electrochemical NR measurements, Hüger *et al.* studied lithium transport in silicon using a multilayer structure consisting of repeated ^{6}LiNbO$_3$/Si/^{natural}LiNbO$_3$/Si units.[60,61] which showed superlattice peaks corresponding to the chemical, 2-layer Si/LiNbO$_3$ periodicity and also half-order peaks corresponding to the isotopic 4-layer ^{6}LiNbO$_3$/^{natural}LiNbO$_3$ periodicity. Upon thermal annealing, lithium diffused between the LiNbO$_3$ layers through the silicon layers, resulting in the loss of the ^{6}LiNbO$_3$/^{natural}LiNbO$_3$ half-order peaks. From these data, the diffusion coefficient of Li in silicon was determined to be $(1.0\pm0.6)\times10^{-13}$ cm^2/s. These experiments will be elaborated upon as one of the detailed examples below.

5.5.1.1.2 Li-ion Battery Cathodes

LiFePO$_4$ Cathodes were first investigated in 2010 by Hirayama *et al.* in a study of epitaxial PLD deposited LiFePO$_4$ that utilized both XRR and NR.[23,53] The XRR of the initial sample in air indicated a 2.4 nm thick contamination layer on the surface and showed no significant changes to the LiFePO$_4$ when again measured in air after cycling. XRR measurements in an electrochemical cell (after removing the electrolyte and contacting the surface with a Kapton[62] window) showed effects of the window on the scattering and could not detect any significant changes to the sample. The NR was done *in operando* with Si incident and a thick electrolyte reservoir. The three oscillations seen in the NR data in air were severely suppressed upon adding the electrolyte.

LiMn$_2$O$_4$ The same group investigated the cathode material LiMn$_2$O$_4$.[21] Here, fits to the NR data showed that the LiMn$_2$O$_4$ SLD increased and decreased with the delithiation and lithiation processes, however the thickness of this cathode remained constant within the measurement uncertainty which was relatively large due to the low amplitude of the oscillations due to the large roughness in the sample.

LiMn$_{1.5}$Ni$_{0.5}$O$_4$ Browning *et al.* investigated LiMn$_{1.5}$Ni$_{0.5}$O$_4$ (LMNO) cathode film before and after adding electrolyte and after oxidation (delithiation) to 4.75 V.[22] Their data had much larger amplitude oscillations, corresponding to much sharper interfaces than the previous two studies, allowing them to confirm that the LMNO film became thinner and increased in SLD after oxidation. A 3.3 nm thick surface layer was observed in presence of the electrolyte, which remained the same thickness and SLD within uncertainty upon reduction the LMNO film. However, since the data obtained on this sample in air prior to insertion in electrolyte were not comprehensively fit to models that included the surface, it is not clear when it formed.

LiCoO$_2$ Most recently, NR was used to study the interface at LiCoO$_2$ (LCO) thin films oriented with the (104) plane exposed to solution.[54] The as-prepared sample had a 0.9 nm surface layer of Li$_2$CO$_3$ or LiOH formed by the reaction with moisture and carbon dioxide in air. When it was brought into contact with the solution, the surface layer apparently became much thicker, 30.6 nm, and rougher, limiting the features in the NR.

The cathode studies may be classified into two groups, those which report a thick SEI (LiFePO$_4$, LiMn$_2$O$_4$, LiCoO$_2$), and one with a thinner SEI that does not change thickness with potential (LiMn$_{1.5}$Ni$_{0.5}$O$_2$). The larger roughness in the thicker cases increases the uncertainty of the information that can be obtained. No systematic studies have yet been done to determine if this is an intrinsic effect or due to differing experimental procedures by the different research groups.

5.5.1.2 Fuel Cells—Nafion

In the area of fuel cells, NR has been used to investigate the interface between Nafion (the membrane used in polymer electrolyte membrane fuel cells) and several solids at varying degrees of ambient humidification.[15,62,63,64,65,66,67,68] Nafion is a copolymer consisting of a perfluorinated alkyl backbone and sulfonate-functionalized side-chains.[69] The latter make the polymer a cation conducting membrane. The hydrophobic perfluorinated backbone domains and hydrophilic sulfonate groups phase segregate, with the latter forming a cation-conducting network of inverted micelles connected by channels.[69] The degree of hydration affects the structure and the ionic conductivity.

NR has been used to investigate the interaction of Nafion with various substrates, including silicon oxide,[63] organosilicate glasses of varying degrees of hydrophilicity,[67] Pt and Au thin films,[15,63] and glassy carbon.[64] It was found that the interaction of sulfonate groups with hydrophilic substrates leads to the formation of lamellar structures with alternating hydrophilic and hydrophobic domains (alternating low and high SLD layers, respectively, with hydration).[12,63,65,67] These layered structures persist even when the film is dehydrated. The use of contrast variation to determine the depth profile of the three separate phases; water, fluorocarbons and sulfonate groups will be presented as one of the detailed examples below. In contrast, only a single water rich layer formed at Au and Pt surfaces.

A study using D_2O to hydrate Nafion films indicated a hydrated layer adjacent to the vapor interface and a hydrophobic (lower SLD) region adjacent to Pt on an as-prepared Pt film on a glassy carbon substrate.[64] For an electrochemically oxidized Pt film, there was instead a D_2O-rich Nafion layer at the interface with Pt and a water poor layer adjacent to the vapor phase. For a Nafion film on glassy carbon, the data were fit with a three-layer model with hydrophilic (higher SLD) regions adjacent to the Nafion/carbon and Nafion/air interfaces.

5.5.1.3 Capacitor

There is one example of NR used to characterize a supercapacitor electrode. Vezvaie studied a thin film Co_3O_4 in 0.01 mol/L potassium hydroxide solution.[70] Initially, two measurements were made in air, one with air as the incident medium and the other in back-reflectivity mode with silicon as the incident medium. Measurements were then made in three different (electrolyte-free) H_2O/D_2O mixtures of differing SLD in an attempt to match the SLD of the Co_3O_4 layer. These measurements suggested the presence of a surface layer with a SLD slightly lower than that of the bulk, which was attributed to either contamination or possibly nano-bubbles or orientationally constrained water molecules. The SLD of the cobalt oxide layer increased when brought into contact with (mostly deuterated) water, indicating a reaction (*e.g.* forming CoOOD or $Co(OD)_2$). No significant change occurred when the electrode was brought into contact with KOH-containing solution. When a potential of +1 V vs SCE was applied to the working electrode, the SLD of the Co_3O_4 increased and the surface layer was removed. The increase in the SLD during the potential hold at +1 V *vs* SCE suggests greater incorporation of deuterium into the film (*e.g.* through further CoOOD formation). When the electrode was released to open circuit again, the SLD of the Co_3O_4 layer returned to the original value in solution and a surface layer of SLD slightly higher than the bulk Co_3O_4 and SLD-matched solution was present. These changes indicate a chemically reversible reaction in the Co_3O_4 film attributed to Co hydroxide and or oxyhydroxide, and a chemically irreversible reaction in the in the contamination layer. The data also indicate that the entire thickness of the film is altered in the electrochemical reaction, rather than only a surface layer being active.

5.5.1.4 Aqueous Battery Cathode

There is an example of NR used to study nickel hydroxide, an aqueous cathode material, *in situ*.[71] Nickel hydroxide/oxyhydroxide-based materials are the cathode used in nickel metal hydride and nickel cadmium cells. When nickel hydroxide is oxidized and reduced, charge balance is maintained in the material by insertion and removal of hydrogen ions. Water can also intercalate into nickel hydroxide

25

films, particularly the disordered α/γ phases. The SLD of the film is thus expected to vary with oxidation state.

A nickel hydroxide electrode was prepared by electrochemical precipitation from a 0.1 M $Ni(NO_3)_2$ solution onto a gold film and then transferred to a 1 mol/L LiOH solution in D_2O for NR measurements. NR was measured at a fixed angle just above the critical angle while the potential was cycled. It is not possible to fit the NR data at a fixed angle for a monochromatic instrument, though simulations indicated that the reflectivity at this angle would vary in approximately a linear manner with the SLD of the nickel hydroxide film. The advantage of this data collection strategy is better time resolution, though it sacrifices the ability to fit the data to a model to determine a thickness/composition profile. The reflectivity had an approximately linear dependence on the amount of charge passed. This was attributed to expulsion of deuterium with oxidation, though Li^+ insertion was also considered a possibility (however this is unlikely during oxidation). In one complete potential cycle, a net oxidative charge was passed (*i.e.* there was coulombic inefficiency), and the reflectivity did not return to its original value. This was attributed at least in part to trapping of some nickel with an oxidation state greater than +2 in the film.

5.5.1.5 Non-energy storage/conversion electrochemistry

There are a few publications which study the growth of oxides on refractory metals in aqueous media including titanium[13,17] and zirconium.[72] Reductive hydrogen absorption was also studied in the latter case,[72] as well as in another paper considering titanium.[73] The corrosion behavior of nickel has also been studied in mildly acidic chloride-containing aqueous media.[74]

5.5.1.6 Redox Active Polymers

There are also several papers regarding redox active polymers, including electropolymerized conducting polymers[75,16,76,77,78,79,80] and polymers functionalized with redox-active groups.[81,82,83,84,85,86] One example is polyvinyl ferrocene (PVF),[84,85,86] which has been considered as a lithium ion battery electrode,[35] amongst other possible uses. The electrochemical behavior of electroactive spin-cast PVF films was investigated in a series of NR measurements in aqueous sodium perchlorate solutions. The initial study considered equilibrated films at constant potentials with different concentrations of supporting electrolyte.[84] In subsequent studies, a novel technique which allowed NR to be measured under potentiodynamic conditions was used.[85,86] While the electrode potential was cycled, the NR data was sorted into bins spanning different segments of the potential sweep using a boxcar averaging technique on a TOF instrument. The bins covered either 20 mV or 50 mV potential ranges.[85,86] This type of measurement requires a system that undergoes very little change with cycling.

A PVF film with a capacity of about 1.75 mC/cm^2 and about 37 nm thick in the reduced state was studied at 1 mV/s.[86] The film expanded upon oxidation and contracted upon reduction in approximately a linear manner with charge passed (~0.2 nm/mC). In the reduced state, the ferrocene groups of PVF are neutral, but become positively charged with oxidation. To maintain charge neutrality, anions enter the film. The anions may remain solvated to some degree when entering the film. Contrast variation measurements were made with D_2O and H_2O solutions, which allowed the degree of film solvation to be determined. In the reduced state, the film contained about 1 molecule of water per ferrocene group. Upon oxidation, this increased to about 4.5 water molecules per ferrocene group, with most of the change taking place during the passage of the first 25% of the oxidation capacity of the film. Based upon the molar volume of water and the perchlorate ionic radius, the swelling of the film with oxidation was not as great as would be expected. This was taken to indicate that there was void space in the reduced state of the film that is inaccessible to water, possibly due to greater hydrophobicity.

Measurements were also carried out at 10 mV/s. In this case, there was found to be more solvent remaining in the film in the reduced state than with the slower measurement. The SLD profile varied

26

less homogeneously with oxidation and reduction at this higher sweep rate, and this was taken to indicate the anion movement was slower than electron transport within the film. Also, the film lost some capacity with cycling at the higher sweep rate, and the decreased film thickness measured with NR suggested this may have been due to loss of some of some material from the film.

5.5.2 Examples

Three different examples are chosen to highlight several advantages of Neutron Reflectometry that can be applied to green energy systems. In the first the use of *in operando* electrochemistry is demonstrated through clear characterization of changes in the structure and composition of the SEI layer as a function of potential within a cycle and with number of cycles. In the second example, a detailed depth profile of composition at the interface between Nafion, a polymer electrolyte, and a hydrophilic surface is obtained using isotope substitution of water. Finally, isotopic contrast variation is used to measure the tracer diffusivity of Li in Si.

5.5.2.1 In Operando Neutron Reflectometry Measurement of the Evolution of the Solid Electrolyte Interphase in Li-Ion Batteries with potential and number of cycles

Owejan *et al.* used *in operando* NR to systematically characterize the evolution of the SEI structure as a function of potential and number of potential cycles on an anode-approximating working electrode.[20] To enhance the sensitivity of the measurement to the SEI a non-intercalating working electrode, Cu, was selected. This ensured that all the changes to the NR would be associated with the evolving SEI layer, and not with changes to the working electrode itself due to Li absorption. Furthermore, the total charge passed could be associated with the electrolyte breakdown. Cu could also be made with sufficient smoothness to avoid averaging over a thin SEI that could potentially be as thin as a few nanometers by allowing useful measurements to $Q>1.5$ nm^{-1}. The electrolyte consisted of 1 mol/L LiPF$_6$ in a 1:2 (v/v) mixture of ethylene carbonate-d$_4$ and diethyl carbonate. The ethylene carbonate was fully deuterated to increase the SLD of the electrolyte and thus increase its contrast with and sensitivity to the SEI (which was expected to have a low SLD due to the presence of ^{1}H from the DEC and particularly Li). The deuterated solvent also has the added benefit of decreasing incoherent scattering, thus decreasing the background and allowing measurements to higher Q values.

NR data (Fig. 5.3), collected at each fixed potential, was initiated after the current had decayed. NR data was taken as a series of specular scans, which were compared to ensure that the sample structure did not change to within statistics over time. Scans that did not vary from one another were subsequently combined to reduce measurement uncertainty. Therefore, the duration of the reflectivity data collection is not believed to affect the interface structure being studied. Throughout the experiment the current was recorded and the integrated charge at each test point was determined. Model selection was aided by a simultaneous fit of the initial two data sets; one with the sample at open circuit, and the other after 10 potential cycles to form an SEI layer. This simultaneous fit reduced the uncertainty in the model and more accurately determined the structure of the underlying layers including the Cu electrode and the Ti adhesion layer.

Detailed statistical methods were used to demonstrate the accuracy of the fits, including χ^2 values below 1.59, a Bayesian comparison of fits between models with and without the SEI layer included, and 68% confidence intervals determined form Monte Carlo fitting techniques reported for both the fitted parameters and the best fit-determined SLD profiles. These validate the accuracy to which the presence of the SEI layer is demonstrated and show sufficient sensitivity to how it differs at various potentials and number of cycles. The NR results were combined with *in operando* electrochemical measurements and careful post-mortem measurements to provide a more detailed discussion of the structure of the SEI and an interpretation of the processes that occurred.

In particular, the NR measurements were first taken in the presence of electrolyte at open circuit, which revealed the presence of a 7 nm-thick layer, likely consisting of Cu carbonate and copper

27

hydroxide. After 10 potential cycles, ending with a hold at 0.25 V *vs* Li/Li$^+$, the initial layer was removed and a 4.0 nm SEI was observed (which is similar in thickness to the SEI observed in several other studies.   The next NR data was taken while holding at 0.15 V after 10 more potential cycles. Here it was found that the SEI had grown to 4.5 nm and had a nearly identical SLD. Subsequently, the potential was ramped to sequential test points corresponding to oxidation and reduction peaks and other points determined from the voltammogram. These measurements revealed a SEI layer that increased in SLD (lost Li atoms) as the potential was raised to the first oxidation process at 1V, then became thinner at 2.3 V, beyond a second oxidation process. Upon decreasing to 1.5 V, the SEI grew considerably in thickness with a much higher relative SLD as the potential dropped below the first reduction peak, presumably by adding material poor in Li at potentials where the electrolyte first became unstable. Lowering the potential to 0.8 V resulted in no significant change to the SEI as expected from the lack of features in the voltammogram in this range. Then, as the potential was sequentially lowered to 0.25 V then 7 mV the SEI increased in thickness and roughness with lower SLD preferentially at the electrode side of the SEI, as presumably more Li was added. This final SEI was 8.9 nm thick but with a substantially increased surface roughness, perhaps due to the prolonged holds at intermediate potentials. Decreased amplitude of the features in the CV with SEI growth confirmed the passivating nature of the SEI. In addition, post mortem XPS measurements established candidates for the composition of the final SEI. The volumes of each of these were adjusted to match both the SLD and thickness measured by NR at each test point. The charge associated with the formation of this suite was calculated for each test point. For earlier test points, roughly twice as much charge was measured compared to the amount needed to form the suite of molecules determined by the modeling. This ratio increased to a factor of five for later scans. This indicates that most of the species generated by reducing the electrolyte do not contribute to formation of the SEI (Fig. 5.3).
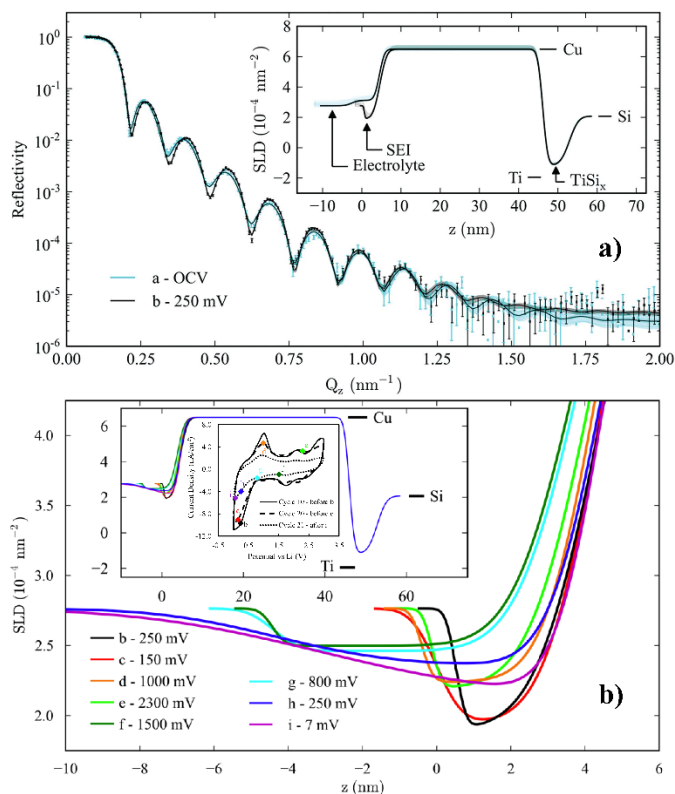
Figure 5.3: a) Neutron reflectivity of a thin-film copper electrode in a 1 mol/L LiPF$_6$ in ethylene carbonate-d$_4$ and diethyl carbonate (1:2 vol./vol.) solution at open circuit and then held at +0.25 V *vs* Li/Li$^+$ after 10 potential cycles. The inset shows the SLD profiles determined by a simultaneous fit to the data. In both, the darker and lighter shaded bands represent the 68% and 95% confidence intervals respectively. b) Nested inset: cyclic voltammogram of the copper thin film electrode showing selected cycles at 10 mV/s. Test points b-i denote the locations of potentiostatic holds for NR measurements. b) A portion the SLD profile as a function of depth for the SEI deposited on Cu, showing the evolution of the thickness, SLD, and interface roughness with the potential at which the electrode was held indicated. Lines for b-i are the best individual fits, with several parameters kept constant at values determined from the simultaneous fit of the OCV and +0.25 V data (see text for details). The first inset shows the full SLD profile, with the fits co-aligned on the Ti layer.[20]

5.5.2.2 Detailed investigations of phase segregation in polymer electrolytes.

Nafion has become the most widely used polymer electrolyte in PEM fuel cells because of its high proton conductivity, structural properties, and low permeability to fuel and oxygen. It is composed of a perfluoroethylene backbone with perfluorinated vinyl ether side chains that are terminated by sulfonic acid groups. When hydrated, the hydrophobic backbone phase-segregates from the water, with the sulfonic acid groups at the interface. In a fuel cell, H ions are transported through these interconnected ionic domains. However, the morphology of the ionic domains is poorly understood, with a variety of models that fit the small angle scattering data.[69,87,88] Recently cryo TEM has indicated that the structure resembles an interconnected network of ribbon-like ionic domains.[89] In addition to the complex bulk structure, it was discovered[63] that while a single water rich layer forms at the interface with metallic surfaces (*e.g.* Au and Pt) the ionic domains re-arrange into a multi-lamellar structure near hydrophilic substrates, both the native oxide on Si in the original study and other hydrophilic materials *e.g.* organosilicate glass.[67] These multi-lamellar structures may have relevance to the water retention effects of hydrophilic fillers[90,91] and to transport within the nanoscale Nafion coatings that surround the Pt nanoparticle catalyst and their carbon black supports in fuel cell catalyst layers. The spontaneous formation of these lamellae complicates the structural analysis since the number of layers in the sample must first be determined, as in the example above and other green energy thin film systems.

DeCaluwe *et al.* sought to further characterize these lamellae in three ways.[12] Statistical methods were used to determine not only the best fit, but the best model (including the number of layers). Comparing the structure observed for samples with two very different thickness helped verify the model, by diminishing the possibility that the fit represented an incorrect symmetry-related model. Finally, isotopic substitution quantified the depth profile of the water content including lamellae, and also determined the SLD profile of the remaining material.

Two samples, with Nafion content equivalent to thicknesses of 42 nm and 5 nm were prepared using standard spin coating techniques, annealed at 60 °C to ensure bonding, and loaded into a custom designed sample environment that would control temperature and relative humidity to within 0.2 °C and 1.5%, respectively. Because of Nafion's slow uptake of water, repeated reflectivity scans were compared, and only data taken after the sample was verified to be at equilibrium water content was retained. Background scattering was measured and subtracted, for a useful Q range of 0 nm^{-1} to 4.0 nm^{-1}.

The 42 nm sample was measured in a relative humidity, RH = 92% H$_2$O and, after dying, in RH = 0% (in Ar gas). A series of models, each with increasing number of independent lamellae, n, were fit to the data. The χ^2 values decreased with n, up to 6 and 3 layers for RH = 92% and 0% respectively, and were roughly constant for larger n, *i.e.* additional layers did not help the fit. Also the Bayesian Information Criteria, BIC, had a minimum for 6 and 3 layers, confirming that they were the statistically best models. As a further check, an additional model which could accommodate any number of layers with a fixed number of parameters within a single model was used to fit the data. This "damped oscillator model" implicitly supported the observed structure with composition variations of the lamellae decreasing from nearly pure water and pure Nafion near the interface toward an intermediate water volume fraction for the remainder of the film. The SLD of the water rich layers (and separately the Nafion rich layers) as a function of layer number were fit to exponential decay functions, as in a damped oscillator. Similarly, to allow for variations in the thickness of the Nafion rich and water rich layers, they were fit to functions that allowed a geometric increase or decrease with distance from the SiO$_2$ interface. The SLD of the layers were found to significantly vary from remainder of the film only for the first 6 and 3 lamellae in agreement with the independent layer series of models. Furthermore, the entire SLD profile of the best fit to this model was compared to the profile of the best independent lamellae model and were found to agree within the 1 sigma uncertainty bands, for both humidities. This confirms that these fits accurately describe the
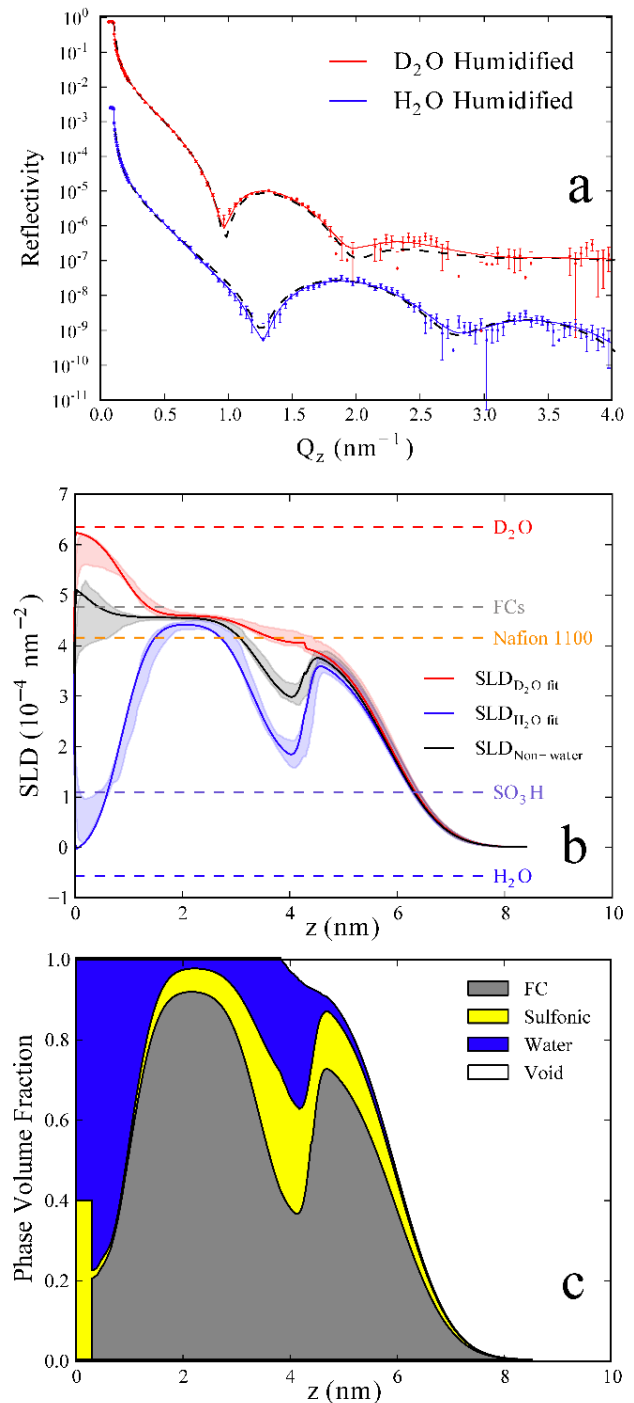

Fig. 5.4: a) Neutron reflectometry data for a ~5nm (dry thickness) Nafion film on Si, humidified in H$_2$O and D$_2$O vapor at RH = 92%. b) Composition depth profiles from a simultaneous fit to the data and the non-water SLD profile (black) determined from the two SLD profiles. Solid lines show best fits and shaded regions show 68% confidence intervals. Dashed lines show known SLDs for constituent molecular groups. (c) Volume-fraction depth profile for the physical model. Here, Nafion bonds to the SiO$_2$ substrate via the -SO$_3$H side-chain terminal groups, with the side-chains stretched across the water-rich first lamella.[12]

individual lamella thicknesses and compositions as well as the damped oscillator model of the composition variations.

The 5 nm sample, also measured in H_2O vapor at RH = 92%, had a lamellar structure very similar to that of the 42 nm sample. This indicated not only the lack of finite size and surface effects but also supported the accuracy of the measurement, model and best fits. In addition, isotopic substitution of the H_2O for D_2O water, was applied to analytically determine the depth profile of the water volume fraction of the thin film. A simultaneous fit of these two data sets was used to provide more accurate SLD profiles for the two cases. By subtracting the two SLD profiles, the depth profile of the water volume fraction was derived, confirming that the SLD variations are due to water rich lamellae and not simply density variations. In addition, the SLD depth profile of the remaining material was obtained. The variations in SLD of this profile indicated that the composition of this remaining material was not uniform. Assuming the bulk SLDs of the two components of Nafion, fluorocarbons and sulfonic acid, and maintaining the known stoichiometry to provide sensitivity for layers below the effective resolution of NR, a detailed nanoscaled depth profile of the phase segregation of the Nafion within the lamellar structure was determined (see Fig. 5.4). This structure includes $-SO_3H$ side-chain terminal groups bonded to the SiO_2 substrate, with the attached side chains spanning across the first water rich lamellae. The first Nafion rich layer consists of hydrophobic fluorocarbon backbones expelled from the water rich region, which in turn expel the additional layers of sulfonic acid groups to the next layer, which attracts water, thus establishing an alternating phase segregation between water-rich and water-poor lamellae, with $-SO_3H$ groups lining the interfaces between.

Finally, to investigate the lamellar structure that is observed for a dried sample, its fitted SLD profile was compared to the SLD profile derived from the humidified sample by removing the water, which both increased the SLD and decreased the thickness of layers in proportion to the water volume fraction. These two profiles were very similar, having nearly the same layer thickness, but with fitted profile having smaller layer to layer SLD variations than the "water removed" model. Since the model retained the entire phase segregation of sulfonic acid and fluorocarbons seen when hydrated, the lower amplitude of SLD variations indicated partial, but not complete interdiffusion of the fluorocarbon and sulfonic acid phases during the 1 hour anneal at 60 °C that was used to dry the sample.

This example highlights the utility of the quantitative nanoscale SLD depth profile obtained by NR when care is taken to establish the uniqueness of the model, the power of isotopic substitution to determine single component depth profile, and the ability to use an SLD depth profile to determine the depth profile of two known phases.

5.5.2.3 Studies of Diffusion using isotopic labelled Lithium

In two related papers, Hüger *et al.*, use isotopically labeled Li to study its diffusion through Si thin films.[60,61] In this example the choice of the isotope not only controls the contrast, but also allows the investigation of diffusion in a material system under chemical equilibrium (after minor transients). The multilayer samples consisted of five repeats of 4 layers: Si, $^6LiNbO_3$ (92% ^6Li isotopic purity), Si, $^{nat}LiNbO_3$ Si (where ^{nat}Li is $^7Li_{0.9}{}^6Li_{0.1}$). These samples produce a large diffracted intensity in the Bragg peak arising from the 2-layer chemical periodicity due to large contrast between Si and either form of $LiNbO_3$. Additionally, due to the large isotopic difference in the scattering length for Li, there is also a large half order peak corresponding to the 4-layer periodicity. As the sample is heated, the two isotopes are exchanged between the reservoirs of the two isotopes of Li, decreasing the isotopic dissimilarity of the two reservoirs and thus the half order peak intensity, which is used to measure the diffusion constant. By moving Li between chemically equivalent full reservoirs, rather than from a full to an empty reservoir, this approach also eliminated the effects of variation in chemical stoichiometry, density, and unit volume (with its related degradation paths) on the structure which would have affected the transport properties and the interpretation of the SLD of the materials.

31

The multilayer samples were deposited by ion beam sputtering, and carefully pre-characterized to determine the composition of interfacial layers that spontaneously formed. This ensured that the correct model was fit to the data and provided an accurate description of intervening layers through which Li must diffuse which greatly improved the understanding of the transients that were observed during the approach to chemical equilibrium. Cross sectional scanning electron microscopy, SEM images showed the distinct layer structure and Auger Electron Spectroscopy (AES) further identified a 2-3 nm thick Li-Si-O interfacial layer. This was confirmed by Fourier transform infrared (FTIR) spectroscopy. The isotopic concentrations, as well as the Nb and Si composition modulations were confirmed with secondary ion mass spectroscopy (SIMS) depth profiling.

In the first study, the intended thicknesses were 10nm of Si and 15nm of $LiNbO_3$, which, due to interfacial reactions upon deposition, formed 10.5 nm of Si surrounded by two 2.4 nm $Si_2Nb_2O_3$ interface layers, separated by 13.7 nm (12.5 nm) of $^{nat}LiNbO_3$ ($^6LiNbO_3$). NR data was collected out to a Q of ~0.3 nm^{-1}, enough to observe both the half and full order Bragg peak. The sample was annealed at 225 °C for 10 min, 45 min, 2 h, and 12 h and returned to room temperature after each annealing for measurement. For all measurements, the chemical Bragg peak had the same integrated intensity and height, indicating that the chemical modulation remained unaltered. After 10 min of annealing, the half order peak was also the same as the initial condition, indicating that for this time period no isotopic intermixing had yet occurred (during which the intervening Si layers absorb a small amount of Li and the system approaches chemical equilibrium). Thereafter half order peak intensity decreased monotonically.

The ^6Li and ^7Li concentrations in their respective reservoirs were determined by fitting the NR data. These concentrations vs. time were fit to exponential decays, which determined the lag time to be $(9 \pm 2) \times 10^2$ seconds. The exponential decay constants were also determined, which yields the permeability, $P = (1.3 \pm 0.2) \times 10^{-17}$ cm^2/s which is the same for both isotopes. Using a solubility S from the literature, the tracer diffusivity was estimated to be $D_S = P/S \approx (6 \pm 2) \times 10^{-14}$ cm^2/s.

The second experiment was enhanced by using the Amor (Apparatus for Multi Option Reflectometry) reflectometer with the Selene option, which allows multiple incident angles to be measured simultaneously.[92,93] This provides much higher flux with a simultaneously measured range of Q values. NR could be measured for a small, 2 mm × 10 mm sample in roughly 2 minutes out to $Q \approx$ 0.6 nm^{-1}, which was far enough to include the first 2 chemical Bragg peaks. Therefore, the sample could be measured at the annealing temperature in real time for various snapshots of time ranging from a 1 to 120 minutes. This *in situ* approach avoided the complications with accounting for diffusion during cool-down and re-heating of the sample, and allowed for measurement on shorter time scales and with more test points. Background scattering with the multi-beam approach was estimated by measuring an empty sample holder. The sample was similar to the one used in the first experiment, with 5 repetitions of the [$^6LiNbO_3$ (18 nm) / Si (9 nm) / $^{nat}LiNbO_3$ (18 nm) / Si (9 nm)] unit. Upon fitting it was determined that the thicknesses were Si (5 nm), with $Li_2Si_2O_5$ (1.8 nm), and $LiNbO_3$ (16.7 nm) for both isotopes of Li.

Again, only the half order peak changed with annealing time. The rest of the reflectivity curve, including critical edge, both chemical Bragg peaks and the intensity between the Bragg peaks remained the same, indicating that the chemical structure including interface widths remained constant during the experiment, and that potential effects of sample warping with heating and prolonged annealing were not present in this case. This was corroborated by measurements at room temperature before and after annealing. The integrated intensity of the half order peak, which is linearly proportional to contrast, or relative isotope abundance, was plotted as a function of time. The fraction of ^6Li/ total Li in the reservoir that was initially ^6Li rich was determined by fitting the NR data. The time-dependence of this fraction was then fit to an exponential decay, yielding a permeability of $P = (2.8 \pm 0.3) \times 10^{-17}$ cm^2/s, and a tracer diffusion coefficient of $D = (1.0 \pm 0.6) \times 10^{-13}$ cm^2/s at 240 °C, which is in good agreement with the $D_S \approx (6 \pm 2) \times 10^{-14}$ cm^2/s at value obtained at 225 °C in the first experiment.

While not discussed, the greater time resolution allowed better investigations of the time lag observed in the first experiment. While the first experiment included a 15 min lag, during which the isotopic ratio remained roughly constant, in the second experiment the greater time resolution showed that there was possibly a more rapid exponential decay to a plateau of approximately 82% ^{6}Li over the first roughly 15 minutes, however this deviation from a single exponential decay (which was fit to the data) was within the error. It is possible that the higher temperature of the second experiment decreased the time lag disproportionally compared to the diffusion.

As mentioned in Section 5.3, measuring a sample that is changing over time could induce a misinterpretation of the structure in that the time average reflectivity curve may not correspond to the scattering from the time average structure. However, in this case two aspects of this experimental design minimize these effects. Because all Q were measured simultaneously rather than in series, the reflectivity curve does not have a Q vs. time dependence which can cause spurious layers to appear in fits. Furthermore, the chemical structure is shown to be invariant after the transients occur, so the only effect is the intensity of the half order peak. While averaging over time of an exponentially decaying intensity does not exactly give the intensity at the average time, it is a small effect that for short time integrations

This third example demonstrates the power of isotope labelling made possible by the scattering lengths for neutron reflectometry. In addition, the ease of implementing *in situ* neutron sample environments and rapid data acquisition rates over a limited required Q range allows for measurements to be made in real time during annealing. Finally, by choosing a sample in which the chemical structure remained constant while only the isotopic concentrations varied allowed accurate measurements of the neutron reflectometry in a time varying system. Combined, these resulted in the precise determination of the tracer diffusion constant for Li in Si.

5.5.3 Summary

Numerous examples in the literature point out the usefulness of Neutron Reflectometry for studies of structures related to green energy applications. These examples benefit from the many advantages of neutron scattering, including the large variations in neutron scattering length for isotopes, particularly of H and Li, which are of interest to energy applications. This control of contrast enables self-diffusion studies and has been used to enhance contrast to layers of interest, for example the SEI, using proper selection of isotopes for components of the electrolyte. Also, contrast variation has been used to obtain precise depth profiles of a given phase, *e.g.* water volume fraction in polymer electrolytes. Moreover, robust and realistic *in operando* sample environments, such as electrochemical cells, are made possible by the large penetration lengths of neutrons to many materials. Studies successfully employing these have provided nano-scaled structural information for unperturbed structures, in their native environments at applied potentials. This not only removes the ambiguities caused by processing required for post mortem measurements but also provides access to non-equilibrium samples. For future studies of green energy systems Neutron Reflectometry can provide unique opportunities and perspectives.

5.4 CONCLUSIONS

Neutron reflectometry has been demonstrated to be a technique capable of providing unique benefits for studies related to nanolayer research in green chemistry. Proper application of this technique can be used to obtain accurate depth profiles with sub-nanometer precision under *in operando* condition of active material in their native environments. This chapter strives to elucidate this lessor known and underutilized technique by providing an introduction, practical guide, examples, and best practices, with the goal of bringing these opportunities to a larger audience. While there remain

numerous opportunities to apply the demonstrated techniques to a greater number of similar experiments, future enhancements to the technique will also allow a greater diversity of applications.

One of the largest future challenges will be to extend the Q-range of the measurements, so that smaller feature sizes can be discernable. Currently this is limited by the signal to noise ratio at higher Q where the reflectivity is low, rather than by the flux of the source. Signal to noise is dominated by isotropic scattering from the sample itself, predominantly liquid reservoirs, or absent this, from the substrate itself. Decreasing the noise will require some means to decrease the thickness of these components, or to distinguish and reject the isotropic scattering and retain the specular. The current method of isolating the specular intensity by subtracting the background (measured away from the specular conditions) is of limited value due to counting statistics. Inordinate time is requires to achieve useful uncertainties as the difference between the specular reflection and background becomes small.

While extending the Q range may prove challenging, recent and planned developments are targeted toward much greater throughput, through shorter acquisition times and more effective data analysis. Several approaches have been are reviewed,[94] and new reflectometers such as Amor with the Selene enhancement[6,92,93] and Candor apply multiple beams (and in the case of Candor also multiple wavelengths with a continuous source) , to increase the effective flux on the sample, allowing for much quicker measurements. This greater throughput will not only allow more measurements to be made, but will also allow studies of kinetics on increasingly shorter timescales or studies of less stable samples, opening up additional possibilities for investigations. Advances in data fitting will allow the researcher to more quickly and efficiently determine the correct model corresponding to the sample structure, and thus decrease the time required to correctly fit the data, keeping up with the greater pace of data collection. Some data collection and fitting techniques (for example the expanded use of reference layers and model independent profiles) will also increase the ease of analysis and help provide unique solutions and thereby decrease the level of experience required to ensure that the results accurately represent the structures that exist in the samples.

In addition, more sophisticated sample environments (for example automated fluid and sample changers, and more stable and easy to assemble electrochemical cells) will help researchers better utilize the increases in throughput. Multimodal measurements (*i.e.* simultaneously performing a second type of measurement while taking NR data) is another advance that will increase the utility of neutron reflectometry. In particular, measurements capable of determining composition, (crystallographic, molecular, and/or atomic) will best complement reflectometry where otherwise, the compositional information is limited to atomic concentrations.

These advances open up numerous new opportunities and applications for an expanding neutron reflectometry user community, as acquisition times get shorter, data fitting becomes easier, and complementary techniques enhance the applicability of the data to a greater diversity of scientific disciplines.

REFERENCES

1. Sears, V. F., *Neutron News* **1992,** *3* (3), 26-37.
2. Majkrzak, C. F.; Metting, C.; Maranville, B. B.; Dura, J. A.; Satija, S.; Udovic, T.; Berk, N. F., *Physical Review A* **2014,** *89* (3), 033851.
3. Majkrzak, C. F.; Berk, N. F., *Physical Review B* **1995,** *52* (15), 10827-10830.
4. Fitzsimmons, M. R.; Majkrzak, C. F., Application of polarized neutron reflectometry to studies of artificially structured magnetic materials. In *Modern Techniques for Characterizing Magnetic Materials*, Zhu, Y., Ed. Springer US: Boston, MA, 2005; pp 107-155.
5. Dubey, M.; Jablin, M. S.; Wang, P.; Mocko, M.; Majewski, J., *The European Physical Journal Plus* **2011,** *126* (11), 110.

6. Stahn, J.; Glavic, A., *Nuclear Instruments and Methods in Physics Research Section A: Accelerators, Spectrometers, Detectors and Associated Equipment* **2016,** *821*, 44-54.

7. Dura, J. A.; Pierce, D. J.; Majkrzak, C. F.; Maliszewskyj, N. C.; McGillivray, D. J.; Lösche, M.; O'Donovan, K. V.; Mihailescu, M.; Perez-Salas, U.; Worcester, D. L.; White, S. H., *Review of Scientific Instruments* **2006,** *77* (7), 074301.

8. Simmons, J. M.; Cook, J. C.; Ibberson, R. M.; Majkrzak, C. F.; Neumann, D. A., *Journal of Applied Crystallography* **2013,** *46* (5), 1347-1352.

9. Neutron Sources. https://www.ncnr.nist.gov/nsources.html (accessed 11/14/2016).

10. Majkrzak, C. F.; Berk, N. F.; Krueger, S.; Dura, J. A.; Tarek, M.; Tobias, D.; Silin, V.; Meuse, C. W.; Woodward, J.; Plant, A. L., *Biophysical Journal* **2000,** *79* (6), 3330-3340.

11. Kirby, B. J.; Kienzle, P. A.; Maranville, B. B.; Berk, N. F.; Krycka, J.; Heinrich, F.; Majkrzak, C. F., *Current Opinion in Colloid & Interface Science* **2012,** *17*, 44-53.

12. DeCaluwe, S. C.; Kienzle, P. A.; Bhargava, P.; Baker, A. M.; Dura, J. A., *Soft Matter* **2014,** *10* (31), 5763-5776.

13. Wiesler, D. G.; Majkrzak, C. F., *Physica B: Condensed Matter* **1994,** *198* (1), 181-186.

14. Berk, N. F.; Majkrzak, C. F., *Physical Review B* **1995,** *51*, 11296-11309.

15. Murthi, V. S.; Dura, J.; Satija, S.; Majkrzak, C., *ECS Transactions* **2008,** *16* (2), 1471-1485.

16. Richardson, R. M.; Swann, M. J.; Hillman, A. R.; Roser, S. J., *Faraday Discussions* **1992,** *94* (0), 295-306.

17. Tun, Z.; Noël, J. J.; Shoesmith, D. W., *J. Electrochem. Soc.* **1999,** *146* (3), 988-994.

18. Lauw, Y.; Rodopoulos, T.; Gross, M.; Nelson, A.; Gardner, R.; Horne, M. D., *Review of Scientific Instruments* **2010,** *81* (7), 074101.

19. Wang, H.; Downing, R. G.; Dura, J. A.; Hussey, D. S., In Situ Neutron Techniques for Studying Lithium Ion Batteries. In *Polymers for Energy Storage and Delivery: Polyelectrolytes for Batteries and Fuel Cells*, American Chemical Society: 2012; Vol. 1096, pp 91-106.

20. Owejan, J. E.; Owejan, J. P.; DeCaluwe, S. C.; Dura, J. A., *Chem. Mater.* **2012,** *24* (11), 2133-2140.

21. Yonemura, M.; Hirayama, M.; Suzuki, K.; Kanno, R.; Torikai, N.; Yamada, N. L., *Journal of Physics: Conference Series* **2014,** *502* (1), 012054.

22. Browning, J. F.; Baggetto, L.; Jungjohann, K. L.; Wang, Y.; Tenhaeff, W. E.; Keum, J. K.; Wood, D. L.; Veith, G. M., *ACS Applied Materials & Interfaces* **2014,** *6* (21), 18569-18576.

23. Hirayama, M.; Yonemura, M.; Suzuki, K.; Torikai, N.; Smith, H.; Watkinsand, E.; Majewski, J.; Kanno, R., *Electrochemistry* **2010,** *78* (5), 413-415.

24. Jerliu, B.; Dorrer, L.; Huger, E.; Borchardt, G.; Steitz, R.; Geckle, U.; Oberst, V.; Bruns, M.; Schneider, O.; Schmidt, H., *Phys. Chem. Chem. Phys.* **2013,** *15* (20), 7777-7784.

25. Topalov, A. A.; Katsounaros, I.; Auinger, M.; Cherevko, S.; Meier, J. C.; Klemm, S. O.; Mayrhofer, K. J. J., *Angewandte Chemie International Edition* **2012,** *51* (50), 12613-12615.

26. Zoski, C. G., Handbook of Electrochemistry. Smith, T. J.; Stevenson, K. J., Eds. Elsevier: 2007; pp 73-110.

27. Ender, M.; Weber, A.; Ellen, I.-T., *J. Electrochem. Soc.* **2011,** *159* (2), A128-A136.

28. Marquardt, D. W., *Journal of the Society for Industrial and Applied Mathematics* **1963,** *11*, 431-441.

29. Nelder, J. A.; Mead, R., *The Computer Journal* **1965,** *7*, 308-313.

30. Storn, R.; Price, K., *Journal of Global Optimization* **1997,** *11*, 341-359.

31. Laub, C. F.; Kuhl, T. L., *The Journal of Chemical Physics* **2006,** *125*, 244702-244702-8.

32. Hastings, W. K., *Biometrika* **1970,** *57*, 97-109.

33. Vrugt, J. A.; Ter Braak, C. J. F.; Diks, C. G. H.; Robinson, B. A.; Hyman, J. M.; Higdon, D., *International Journal of Nonlinear Sciences and Numerical Simulation* **2009,** *10*, 273–290.

34. Lesniewski, J. E.; Disseler, S. M.; Quintana, D. J.; Kienzle, P. A.; Ratcliff, W. D., *Journal of Applied Crystallography* **2016,** *49* (6), 2201-2209.

35. Kienzle, P. A.; Krycka, J.; Patel, N.; Sahin, I. *Refl1D*, 2011.

36. Nelson, A., *Journal of applied crystallography* **2006,** *39*, 273–276.

37. Goodenough, J. B.; Kim, Y., *Chem. Mater.* **2010,** *22* (3), 587-603.

38. Gauthier, M.; Carney, T. J.; Grimaud, A.; Giordano, L.; Pour, N.; Chang, H.-H.; Fenning, D. P.; Lux, S. F.; Paschos, O.; Bauer, C.; Maglia, F.; Lupart, S.; Lamp, P.; Shao-Horn, Y., *The Journal of Physical Chemistry Letters* **2015,** *6* (22), 4653-4672.

39. Peled, E., *J. Electrochem. Soc.* **1979,** *126* (12), 2047-2051.

40. Xu, K., *Chemical Reviews* **2014,** *114* (23), 11503-11618.

41. Fears, T. M.; Doucet, M.; Browning, J. F.; Baldwin, J. K. S.; Winiarz, J. G.; Kaiser, H.; Taub, H.; Sacci, R. L.; Veith, G. M., *Phys. Chem. Chem. Phys.* **2016,** *18* (20), 13927-13940.

42. Fister, T. T.; Long, B. R.; Gewirth, A. A.; Shi, B.; Assoufid, L.; Lee, S. S.; Fenter, P., *The Journal of Physical Chemistry C* **2012,** *116* (42), 22341-22345.

43. Fister, T. T.; Esbenshade, J.; Chen, X.; Long, B. R.; Shi, B.; Schlepütz, C. M.; Gewirth, A. A.; Bedzyk, M. J.; Fenter, P., *Advanced Energy Materials* **2014,** *4* (7), 1301494-n/a.

44. McArthur, M. A.; Trussler, S.; Dahn, J. R., *J. Electrochem. Soc.* **2012,** *159* (3), A198-A207.

45. Dufek, E. J., *ECS Electrochemistry Letters* **2014,** *3* (11), A108-A111.

46. Wagemaker, M.; van de Krol, R.; van Well, A. A., *Physica B: Condensed Matter* **2003,** *336* (1–2), 124-129.

47. Kawaura, H.; Harada, M.; Kondo, Y.; Kondo, H.; Suganuma, Y.; Takahashi, N.; Sugiyama, J.; Seno, Y.; Yamada, N. L., *ACS Applied Materials & Interfaces* **2016,** *8* (15), 9540-9544.

48. Jerliu, B.; Hüger, E.; Dörrer, L.; Seidlhofer, B. K.; Steitz, R.; Oberst, V.; Geckle, U.; Bruns, M.; Schmidt, H., *The Journal of Physical Chemistry C* **2014,** *118* (18), 9395-9399.

49. Veith, G. M.; Baggetto, L.; Sacci, R. L.; Unocic, R. R.; Tenhaeff, W. E.; Browning, J. F., *Chemical Communications* **2014,** *50* (23), 3081-3084.

50. DeCaluwe, S. C.; Dhar, B. M.; Huang, L.; He, Y.; Yang, K.; Owejan, J. P.; Zhao, Y.; Talin, A. A.; Dura, J. A.; Wang, H., *Phys. Chem. Chem. Phys.* **2015,** *17* (17), 11301-11312.

51. Veith, G. M.; Doucet, M.; Baldwin, J. K.; Sacci, R. L.; Fears, T. M.; Wang, Y.; Browning, J. F., *The Journal of Physical Chemistry C* **2015,** *119* (35), 20339-20349.

52. Seidlhofer, B.-K.; Jerliu, B.; Trapp, M.; Hüger, E.; Risse, S.; Cubitt, R.; Schmidt, H.; Steitz, R.; Ballauff, M., *ACS Nano* **2016**.

53. Hirayama, M., *Electrochemistry* **2015,** *83* (9), 701-706.

54. Minato, T.; Kawaura, H.; Hirayama, M.; Taminato, S.; Suzuki, K.; Yamada, N. L.; Sugaya, H.; Yamamoto, K.; Nakanishi, K.; Orikasa, Y.; Tanida, H.; Kanno, R.; Arai, H.; Uchimoto, Y.; Ogumi, Z., *The Journal of Physical Chemistry C* **2016**.

55. Dahn, J. R.; Zheng, T.; Liu, Y.; Xue, J. S., *Science* **1995,** *270* (5236), 590-593.

56. Besenhard, J. O.; Winter, M.; Yang, J.; Biberacher, W., *Journal of Power Sources* **1995,** *54* (2), 228-231.

57. Wagner, M. R.; Albering, J. H.; Moeller, K. C.; Besenhard, J. O.; Winter, M., *Electrochemistry Communications* **2005,** *7* (9), 947-952.

58. Beaulieu, L. Y.; Hatchard, T. D.; Bonakdarpour, A.; Fleischauer, M. D.; Dahn, J. R., *J. Electrochem. Soc.* **2003,** *150* (11), A1457-A1464.

59. Throughout this chapter, u. o. n., all uncertainties and error bars represent one standard error.

60. Hüger, E.; Dörrer, L.; Rahn, J.; Panzner, T.; Stahn, J.; Lilienkamp, G.; Schmidt, H., *Nano Letters* **2013,** *13* (3), 1237-1244.

61. Hüger, E.; Stahn, J.; Schmidt, H., *J. Electrochem. Soc.* **2015,** *162* (13), A7104-A7109.

62. Certain commercial equipment, i., or materials are identified in this paper to foster understanding. Such identification does not imply recommendation or endorsement by the National Institute of

Standards and Technology, nor does it imply that the materials or equipment identified are necessarily the best available for the purpose.

63. Dura, J. A.; Murthi, V. S.; Hartman, M.; Satija, S. K.; Majkrzak, C. F., *Macromolecules* **2009,** *42* (13), 4769-4774.

64. Wood, D. L.; Chlistunoff, J.; Majewski, J.; Borup, R. L., *J. Am. Chem. Soc.* **2009,** *131* (50), 18096-18104.

65. Eastman, S. A.; Kim, S.; Page, K. A.; Rowe, B. W.; Kang, S.; Soles, C. L.; Yager, K. G., *Macromolecules* **2012,** *45* (19), 7920-7930.

66. Eastman, S. A.; Kim, S.; Page, K. A.; Rowe, B. W.; Kang, S.; DeCaluwe, S. C.; Dura, J. A.; Soles, C. L.; Yager, K. G., *Macromolecules* **2013,** *46* (2), 571-571.

67. Kim, S.; Dura, J. A.; Page, K. A.; Rowe, B. W.; Yager, K. G.; Lee, H.-J.; Soles, C. L., *Macromolecules* **2013,** *46* (14), 5630-5637.

68. Kalisvaart, W. P.; Fritzsche, H.; Mérida, W., *Langmuir* **2015,** *31* (19), 5416-5422.

69. Mauritz, K. A.; Moore, R. B., *Chemical Reviews* **2004,** *104* (10), 4535-4586.

70. Vezvaie, M.; Kalisvaart, P.; Fritzsche, H.; Tun, Z.; Mitlin, D., *J. Electrochem. Soc.* **2014,** *161* (5), A798-A802.

71. Saville, P. M.; Gonsalves, M.; Hillman, A. R.; Cubitt, R., *The Journal of Physical Chemistry B* **1997,** *101* (1), 1-4.

72. Noël, J. J.; Shoesmith, D. W.; Tun, Z., *J. Electrochem. Soc.* **2008,** *155* (8), C444-C454.

73. Vezvaie, M.; Noël, J. J.; Tun, Z.; Shoesmith, D. W., *J. Electrochem. Soc.* **2013,** *160* (9), C414-C422.

74. Singh, S.; Basu, S.; Poswal, A. K.; Tokas, R. B.; Ghosh, S. K., *Corrosion Science* **2009,** *51* (3), 575-580.

75. Roser, S. J.; Richardson, R. M.; Swann, M. J.; Hillman, A. R., *Journal of the Chemical Society, Faraday Transactions* **1991,** *87* (17), 2863-2864.

76. Hillman, A. R.; Saville, P. M.; Glidle, A.; Richardson, R. M.; Roser, S. J.; Swann, M. J.; Webster, J. R. P., *J. Am. Chem. Soc.* **1998,** *120* (49), 12882-12890.

77. Hillman, A. R.; Bailey, L.; Glidle, A.; Cooper, J. M.; Gadegaard, N.; Webster, J. R. P., *Journal of Electroanalytical Chemistry* **2002,** *532* (1–2), 269-276.

78. Glidle, A.; Hadyoon, C. S.; Gadegaard, N.; Cooper, J. M.; Hillman, A. R.; Wilson, R. W.; Ryder, K. S.; Webster, J. R. P.; Cubitt, R., *The Journal of Physical Chemistry B* **2005,** *109* (30), 14335-14343.

79. Glidle, A.; Hillman, A. R.; Ryder, K. S.; Smith, E. L.; Cooper, J. M.; Dalgliesh, R.; Cubitt, R.; Geue, T., *Electrochimica Acta* **2009,** *55* (2), 439-450.

80. Veder, J.-P.; De Marco, R.; Patel, K.; Si, P.; Grygolowicz-Pawlak, E.; James, M.; Alam, M. T.; Sohail, M.; Lee, J.; Pretsch, E.; Bakker, E., *Analytical Chemistry* **2013,** *85* (21), 10495-10502.

81. Wilson, R. W.; Cubitt, R.; Glidle, A.; Hillman, A. R.; Saville, P. M.; Vos, J. G., *J. Electrochem. Soc.* **1998,** *145* (5), 1454-1461.

82. Wilson, R. W.; Bailey, L.; Cubitt, R.; Gonsalves, M.; Glidle, A.; Robert Hillman, A.; G. Vos, J.; Hogan, C.; R. P. Webster, J., *Phys. Chem. Chem. Phys.* **1999,** *1* (5), 843-853.

83. Wilson, R. W.; Cubitt, R.; Glidle, A.; Hillman, A. R.; Saville, P. M.; Vos, J. G., *Electrochimica Acta* **1999,** *44* (20), 3533-3548.

84. Glidle, A.; Cooper, J.; Hillman, A. R.; Bailey, L.; Jackson, A.; Webster, J. R. P., *Langmuir* **2003,** *19*, 7746-7753.

85. Cooper, J. M.; Cubitt, R.; Dalgliesh, R. M.; Gadegaard, N.; Glidle, A.; Hillman, A. R.; Mortimer, R. J.; Ryder, K. S.; Smith, E. L., *J. Am. Chem. Soc.* **2004,** *126* (47), 15362-15363.

86. Glidle, A.; Hillman, A. R.; Ryder, K. S.; Smith, E. L.; Cooper, J.; Gadegaard, N.; Webster, J. R. P.; Dalgliesh, R.; Cubitt, R., *Langmuir* **2009,** *25* (7), 4093-4103.

87. Haubold, H. G.; Vad, T.; Jungbluth, H.; Hiller, P., *Electrochimica Acta* **2001,** *46* (10–11), 1559-1563.

88. Rubatat, L.; Rollet, A. L.; Gebel, G.; Diat, O., *Macromolecules* **2002,** *35* (10), 4050-4055.

89. Allen, F. I.; Comolli, L. R.; Kusoglu, A.; Modestino, M. A.; Minor, A. M.; Weber, A. Z., *ACS Macro Letters* **2015,** *4* (1), 1-5.

90. Adjemian, K. T.; Lee, S. J.; Srinivasan, S.; Benziger, J.; Bocarsly, A. B., *J. Electrochem. Soc.* **2002,** *149* (3), A256-A261.

91. Nicotera, I.; Zhang, T.; Bocarsly, A.; Greenbaum, S., *J. Electrochem. Soc.* **2007,** *154* (5), B466-B473.

92. Stahn, J.; Panzner, T.; Filges, U.; Marcelot, C.; Böni, P., *Nuclear Instruments and Methods in Physics Research Section A: Accelerators, Spectrometers, Detectors and Associated Equipment* **2011,** *634* (1, Supplement), S12-S16.

93. Stahn, J.; Filges, U.; Panzner, T., *Eur. Phys. J. Appl. Phys.* **2012,** *58* (1), 11001.

94. Ott, F.; Menelle, A., *The European Physical Journal Special Topics* **2009,** *167* (1), 93-99.